

# Abstract

CELA, CARLOS J. A Multiresolution Admittance Method for Large-Scale Bioelectromagnetic Interactions. (Under the direction of Dr. Gianluca Lazzi.)

The admittance method is a numerical electromagnetic method in which the problem space is discretely partitioned and its electrical properties represented in terms of an admittance network created from the dielectric properties of the intervening materials. In the presence of electromagnetic stimulation, the electrical response of the problem space is approximated as the response of the admittance network to a stimulus representative of the original source. In this work, a three-dimensional multiresolution admittance method adequate for solving large scale bioelectromagnetic models is introduced. The formulation is applied to modeling and simulation of retinal implantable stimulation arrays and electrical injury by electroporation.

A distinctive advantage of using the admittance method for bioelectromagnetic simulations is that the method implies a representation of the system in terms of an electric network. Examples of applications where this method can be of use are the modeling of metal-electrolyte interfaces for implanted electrodes, and the simulation of electrical behavior of neural cells using three-dimensional variations of the core-conductor model. Because arbitrary circuitual elements can be added to an admittance network to model physiological behavior, the admittance method (and its dual, the impedance method) can, in principle, be used to bridge the gap between tissue level and cellular level modeling. Even though numerical treatments of bioelectromagnetic phenomena using the admittance and impedance methods have been available for several decades, detailed modeling of large biological structures has presented unique challenges, as the shapes of anatomical structures tend to be complex, and frequently the sizes of features that must be resolved are small compared to the overall size of the model. The multiresolution algorithm presented in this dissertation addresses these issues by greatly reducing the resulting voxel count while keeping an error comparable to the uniform resolution cases. This is achieved by selectively maintaining high resolutions at material boundaries while progressively increasing voxel size inside large homogeneous volumes. At difference of previous treatments of the admittance method, which solved static or single-frequency (frequency domain) models, the proposed formulation can take advantage of time-stepping to simulate the effect of excitation using signals of arbitrary waveforms.

© Copyright 2010 by Carlos J. Cela

All Rights Reserved

A Multiresolution Admittance Method for Large-Scale  
Bioelectromagnetic Interactions

by  
Carlos J. Cela

A dissertation submitted to the Graduate Faculty of  
North Carolina State University  
in partial fulfillment of the  
requirements for the Degree of  
Doctor of Philosophy

Electrical Engineering

Raleigh, North Carolina

2010

APPROVED BY:

---

Dr. Lianne Cartee

---

Dr. Griff Bilbro

---

Dr. Troy Nagle

---

Dr. Gianluca Lazzi  
Chair of Advisory Committee

UMI Number: 3463689

All rights reserved

INFORMATION TO ALL USERS

The quality of this reproduction is dependent upon the quality of the copy submitted.

In the unlikely event that the author did not send a complete manuscript and there are missing pages, these will be noted. Also, if material had to be removed, a note will indicate the deletion.



UMI 3463689

Copyright 2011 by ProQuest LLC.

All rights reserved. This edition of the work is protected against unauthorized copying under Title 17, United States Code.



ProQuest LLC  
789 East Eisenhower Parkway  
P.O. Box 1346  
Ann Arbor, MI 48106-1346

# Dedication

*To my mother, Adriana.*

# Biography

Carlos J. Cela was born in Buenos Aires, Argentina, in 1967. He began his studies in Electrical Engineering in 1985 at the Universidad Tecnologica Nacional (UTN) in Buenos Aires, to be shortly after drafted into the military (Infantry, Battalion 1, Patricios, Buenos Aires). After serving for almost two years, Carlos was dismissed with honors and founded his first software consulting company while continuing his studies part-time. Carlos relocated to the U.S.A. in 1997, where he founded a second software company, which he spent several years developing and eventually selling. He resumed his studies at North Carolina State University in 2003, and began working as a Graduate Research Assistant in the NC State Wireless and Bioelectromagnetics Research Group in 2004. Carlos graduated *Summa Cum Laude* for his B.S. in Electrical Engineering in 2006, and received his Ph.D. in Electrical Engineering in Spring 2010, from North Carolina State University.

Carlos is a member of Phi Kappa Phi and Eta Kappa Nu, and was recognized as a *National Science Foundation* Graduate Research Fellow in 2006. In 2007, he was selected to participate in the *57<sup>th</sup> Meeting of Nobel Laureates in Lindau, Germany* (19<sup>th</sup> Forum on Physiology and Medicine), and was recognized with a *R&D 100 Award* in 2009 for his research work on implantable retinal prostheses. His current research interests are numerical electromagnetics, bioelectromagnetics, and scientific, distributed, and high-performance computing.

## Acknowledgements

First, I would like to thank and acknowledge the guidance and relentless commitment of my mentor and adviser, Dr. Gianluca Lazzi , who beyond providing encouragement and support through the entire PhD process, helped me discover science, and was patient, trusting, and fair in every imaginable way during all these years. My deep gratitude goes also to Dr. Lianne Cartee for her selfless dedication, help, and insightful comments through my doctoral study, and to Dr Griff Bilbro, Dr. Troy Nagle and Dr. Kevin Gard for their guidance and interest in my work.

The intellectual process is collaborative in nature; completing the graduate program would have been a far more difficult task had it not been for the generous support of my co-authors Dr. Elias Greenbaum, Dr. Raphael C. Lee, Dr. Mark S. Humayun, Dr. John Xie, Dr. Richard Castro, Dr. James Weiland, and many others.

I am deeply grateful for the camaraderie and insightful views provided by past and present fellow research group mates, including Dr. Keyoor Gosalia, Dr. Anand Konanur, Dr. Gaurav Gupta, Dr. Stefan Schmidt, Dr. Vinit Singh, Dr. Ajit Rajagopalan, Srinivas Justi, Nitin Kwatra, Ajeet Ajeet, Patrick Brown, Rebecca Mayhew, Jason Thong, Amit Qusba, Sundar Srinivas, Randall Barlow, Benjamin Gaddy, and Shruthi Soora, while working at the lab, traveling to conferences, or just taking pauses to reflect.

My sincere gratitude goes to Elaine Hardin and to the many other people in the Electrical and Computer Engineering department that were always eager to help me navigate the high seas of the PhD process.

The support of family and friends has been crucial during this time. I am grateful for the unconditional love and unwavering emotional support of my mother Adriana, and for the caring presence of my sister Marta, my grandmother Tita, my cousins, and my aunts. I could not have brought this to closure without counting with the presence of my dear friends Scott Chmelar, Pablo Cornes, Dr. Tran Phu Lan, and Dr. Paula Fernandez. My deepest appreciation goes to Dr. Lei Zheng, Lila Pierce Brown, and Carson Efird; all of them were graciously available in times of need. Lastly, I feel blessed to count with the sweetness, love and support of my fiancée Kim Williams, who is to me a permanent living example of how to fearlessly thread through life on the high road.

# Table of Contents

List of Tables . . . . .	vii
List of Figures . . . . .	viii
<b>Chapter 1 Introduction . . . . .</b>	<b>1</b>
1.1 Background . . . . .	1
1.1.1 Retinal Prosthesis . . . . .	2
1.1.2 Electric Injury of Skeletal Muscle . . . . .	4
1.2 Numerical Methods for Bioelectromagnetics . . . . .	4
1.3 Organization of Dissertation . . . . .	9
<b>Chapter 2 The Admittance Method in Bioelectromagnetic Problems . . . . .</b>	<b>11</b>
2.1 Introduction . . . . .	11
2.2 The Admittance Method for Bioelectromagnetic Problems . . . . .	12
2.3 Modeling the Human Body with the Admittance Method . . . . .	14
<b>Chapter 3 A Three-Dimensional, Time-Stepping, Multi-resolution Admittance Method . . . . .</b>	<b>17</b>
3.1 Introduction . . . . .	17
3.1.1 Modeling and Discretization . . . . .	18
3.1.2 Multiresolution Clustering . . . . .	19
3.1.3 Electric Network Generation . . . . .	25
3.1.4 System Solution . . . . .	30
3.1.5 Static Solution . . . . .	30
3.1.6 Frequency Domain Solution . . . . .	32
3.1.7 Time Stepping Solution . . . . .	33
3.2 Post-processing . . . . .	37
3.2.1 Voltage Interpolation . . . . .	37
3.2.2 Calculation of Current Density $\vec{J}$ . . . . .	38
3.2.3 Calculation of Electric Field $\vec{E}$ . . . . .	38
3.2.4 Calculation Equivalent Resistance . . . . .	39
3.3 Method Verification and Error . . . . .	40
3.3.1 Static Case . . . . .	43
3.3.2 Time Varying Case . . . . .	48
<b>Chapter 4 Applications to Medical Implanted Devices: Retinal Prosthesis . . . . .</b>	<b>51</b>
4.1 Introduction . . . . .	51
4.2 Extraocular Electrical Stimulation . . . . .	53
4.3 Parametric Models for Epiretinal Implantable Electrode Array . . . . .	58



4.3.1	Effect of Electrode Array Lift-Off . . . . .	61
4.3.2	Effect of Electrode Diameter . . . . .	63
4.3.3	Effect of Electrode Current Return Placement . . . . .	66
<b>Chapter 5 Modeling Cellular Lysis In Skeletal Muscle due to Electric Shock † . . . . .</b>		<b>68</b>
5.1	Abstract . . . . .	68
5.2	Introduction . . . . .	69
5.3	Electric Injury Model for Cellular Lysis . . . . .	70
5.4	Experimental Data Fitting . . . . .	74
5.5	3-D Multiresolution Admittance Method . . . . .	76
5.6	Numerical Modeling and Simulation . . . . .	76
5.7	Discussion . . . . .	79
<b>Chapter 6 Conclusion . . . . .</b>		<b>82</b>
<b>References . . . . .</b>		<b>84</b>

## List of Tables

Table 3.1	Static Solution Results. . . . .	44
Table 4.1	Tissue Conductivities at 100 Hz. . . . .	54
Table 4.2	Retinal Layered Model. . . . .	61
Table 4.3	Effect of lift-off on GCL current density magnitude for $5 \times 5$ electrode array of $100 \mu m$ electrodes. Values taken under the central electrode, all electrodes active, injecting $100 \mu A$ each. . . . .	62
Table 4.4	Effect of electrode diameter in GCL current density y magnitude for $5 \times 5$ electrode array. Values taken under the central electrode, all electrodes active, injecting $100 \mu A$ each.. . . .	66
Table 5.1	Calculation of remaining healthy cells after a given number of pulses, starting with $N$ healthy cells, having a fraction $\varepsilon$ of remaining healthy cells lysed every pulse. The general expression (bottom, left) is obtained using mathematical induction. . . . .	72
Table 5.2	Values for 10ms pulses. $ \vec{E} $ is expressed in $V \cdot cm^{-1}$ . $\beta_l$ and $\delta$ are adimensional. . . . .	76
Table 5.3	Tissue Conductivities . . . . .	79

# List of Figures

Figure 2.1	Two-dimensional uniform meshing ( <i>Left</i> ), and expanding grid meshing ( <i>Right</i> ). Note the higher resolution at the top left of the expanding grid plot. The expanding grid is more efficient in terms of computational resources, as it allows finer resolutions in parts of the problem space at the expense of less precise results in other portions of the model. . . . .	15
Figure 3.1	Applying the multiresolution clustering algorithm results in the normalized cases above. The voxel reduction ratio obtained during multiresolution clustering varies depending on model geometry and other constraints described in the Clustering Constraints section. Note how vertices are discarded during the clustering process, leading to a reduced number of node equations in the equivalent electrical network. . . . .	20
Figure 3.2	Discretization procedure, using a 16 x 16 x 1 unit voxel grid for illustration purposes. Three materials are considered in this example, tagged as 0, 1, and 2 respectively. Note that a real model would have to further extend in the the $\hat{z}$ direction to properly account for boundary conditions. Starting from a representation of the model (left), a regular cubic mesh is overlaid, and the center points of each voxel are sampled. Voxels are then considered homogeneous, and different numbers are assigned to each material (right). Dielectric properties are associated to the material number.	21
Figure 3.3	Multi-resolution clustering. Starting from the model of Figure 3.2, boundary voxels are marked using a 'B' character.(A), and a quadrant (octant, if in 3D) of size $S = 2$ is swept through the span of the model (B), clustering voxels inside it that are made of the same material, are not boundaries, and comply with the clustering constraints described in the text (C). Clustering order in this example was first along $\hat{x}$ and then along $\hat{y}$ . The size of the quadrant is doubled (D), and the operation is repeated (E). When no more clustering is possible, the process is complete (F). Result is as shown in Figure 3.4. . . . .	22
Figure 3.4	Result after processing the model presented in Figure 3.2 using the multiresolution algorithm. The voxel count has been reduced by 55% compared to the uniformly meshed model. In larger realistic biological models, voxel count reductions on the order of 80 percent are not uncommon. . . . .	23

Figure 3.5	Transversal slices of multiresolution mesh of a model of a spherical capacitor. The top plot corresponds to a multiresolution mesh having a maximum voxel size of $M = 8$ . The bottom plot is the same case with the addition of two guide points at the terminals of the device, at the center and upper left of the Figure respectively, defined using (3.2) with $a = 0.12$ and $b = 0$ . It can be observed how the mesh gradually coarsens from the guide points. This has the effect of creating a smooth spread of the injected current, lowering the numerical error. . . . .	26
Figure 3.6	Equivalent circuit network topology. Network nodes are congruent with the vertices of each voxel, and network impedances are connected between nodes along each of the edges of each voxel. Each edge impedance accounts for modeling a quarter of the voxel's volume in one direction. If one edge is shared among two or more voxels, the edge impedances for each participating voxel are combined in parallel, effectively averaging dielectric properties for all voxels involved. . . . .	27
Figure 3.7	Network generation. Each single voxel (A) is considered as a linear composition of three orthogonal components (B), and each edge impedance (C) models one quarter of the voxel in a given direction. The complete model (D) is obtained by superposition. . . . .	29
Figure 3.8	Capacitor series linear equivalent. . . . .	35
Figure 3.9	Capacitor parallel linear equivalent model. Equivalent current $I_{eq}$ is calculated using (3.18) . . . . .	35
Figure 3.10	Position for center-face voltages of a voxel. $\bar{V}_{bk}$ , $\bar{V}_{rt}$ , and $\bar{V}_{dn}$ , indicated with arrows in the figure, are in the center of the respective non-visible faces of the voxel. . . . .	40
Figure 3.11	Model for method verification. . . . .	41
Figure 3.12	Overall solution error as a combination of round-off error and truncation error. $h$ denotes the voxel size used in the model. Because of computer memory constraints, in general, simulations tend to operate towards the right of the optimum size. Plot reproduced from [49]. . . . .	42
Figure 3.13	Impedance Method error distribution for the Static Case model and multiresolution clustering having a maximum size of 4. . . . .	45
Figure 3.14	Same case as Figure 3.13, but using guide points. . . . .	45
Figure 3.15	Impedance Method error distribution for the Static Case model and multiresolution clustering having a maximum size of 16. . . . .	46
Figure 3.16	Same case as Figure 3.15, but using guide points. . . . .	46

Figure 3.17	Relative error as a function of the residue stop criteria. All the data points correspond to the static case, using multiresolution clustering with guide points at both the current injection and current return points. The maximum normalized voxel size used for clustering on this simulation set was 16. . . . .	47
Figure 3.18	Relative error as a function of the maximum voxel size allowed for clustering. Using guide points at the source and return allows to keep the relative error low independently of the maximum voxel size, permitting simulation of larger models with the errors closer to the uniform resolution case. . . . .	47
Figure 3.19	Canonical network model for spherical lossy capacitor. . . . .	48
Figure 3.20	Analytical and simulated charging voltages over time for time-stepping test case. . . . .	50
Figure 3.21	Error distribution for the time-stepping simulation. . . . .	50
Figure 4.1	Three-dimensional rendering of partial head model used for calculating extraocular (corneal) electric stimulation. Electrodes were positioned in direct contact with the cornea of the eye, and current return was considered in the temporal aspect of the head, shown in the model as a darker cylinder, towards the left side of the figure.	52
Figure 4.2	Transversal slices of numerical model for extraocular stimulation at the center of the eye ( <i>Left</i> ) and corresponding rendering using the multiresolution algorithm and a maximum voxel size $M = 4$ ( <i>Right</i> ). . . . .	53
Figure 4.3	DTL Plus electrode, courtesy of Diagnosys LLC ( <a href="http://www.diagnosysllc.com">www.diagnosysllc.com</a> ), by its own ( <i>Top Left</i> ), and positioned on eye ( <i>Top Right</i> ). ERG-Jet corneal electrode, courtesy of Fabrinal SA ( <a href="http://www.fabrinal.ch">www.fabrinal.ch</a> ), by its own ( <i>Bottom Left</i> ) and placed on eye ( <i>Bottom Right</i> ). . . . .	55
Figure 4.4	Retinal surface voltage map resulting from extraocular stimulation using DTL Plus electrode. The values at the spherical surface of the retina are mapped to a cylindrical surface which is cut at the nasal aspect and unrolled to a rectangular area. Arrows on eye diagrams on the left indicate approximate position of eye for Y axis (looking towards right eye of patient). Left side of plot corresponds to optic nerve, right side corresponds to the frontal portion of the retina. . . . .	56

Figure 4.5	Retinal surface voltage map resulting from extraocular stimulation using ERG Jet electrode. The values at the spherical surface of the retina are mapped to a cylindrical surface which is cut at the nasal aspect and unrolled to a rectangular area. Arrows on eye diagrams on the left indicate approximate position of eye for Y axis (looking towards right eye of patient). Left side of plot corresponds to optic nerve, right side corresponds to the frontal portion of the retina. . . . .	57
Figure 4.6	Approximation of the activation function resulting from extraocular stimulation using DTL electrode. The values at the spherical surface of the retina are mapped to a cylindrical surface which is cut at the nasal aspect and unrolled to a rectangular area. Arrows on eye diagrams on the left indicate approximate position of eye for Y axis (looking towards right eye of patient). Left side of plot corresponds to optic nerve, right side corresponds to the frontal portion of the retina. . . . .	59
Figure 4.7	Approximation of the activation function resulting from extraocular stimulation using ERG Jet electrode. The values at the spherical surface of the retina are mapped to a cylindrical surface which is cut at the nasal aspect and unrolled to a rectangular area. Arrows on eye diagrams on the left indicate approximate position of eye for Y axis (looking towards right eye of patient). Left side of plot corresponds to optic nerve, right side corresponds to the frontal portion of the retina. The red circle marks anomaly due to pinching of choroid in model, present in both Jet and DTL cases. . . . .	60
Figure 4.8	Model of $5 \times 5$ epiretinal electrode array (not to scale). . . . .	61
Figure 4.9	Effect of lift-off in current density magnitude at GCL. Current density magnitude for electrode array in perfect contact with retinal surface ( <i>Top Left</i> ). Current density magnitude for electrode array lifted $50 \mu m$ from retinal surface ( <i>Top Right</i> ). Current density magnitude as a function of lift-off for $100 \mu m$ diameter electrodes. Value of current density magnitude taken in GCL at center of central electrode of array. All electrodes active, each injecting $100 \mu A$ ( <i>Bottom</i> ). . . . .	64
Figure 4.10	Effect of electrode diameter on current density magnitude at GCL. Current density as a function of electrode diameter. Value of current density taken in GCL at center of central electrode of array. All electrodes active, each injecting $100 \mu A$ . . . . .	65

Figure 4.11	Effect of current return placement on current density magnitude at GCL, for electrode arrays having 1024 electrodes. Active electrodes spell pattern reading "BEML NC State University". All active electrodes are injecting the same amount of current in both plots. Disc shaped current return at the lower right corner ( <i>Top</i> ) produces higher current densities as the top and bottom of electrode array. Bar shaped current return at the right of array ( <i>Bottom</i> ) produces higher current densities on the half of the array closer to the current return. . . . .	67
Figure 5.1	Configuration used for calculating electric field inside upper limb. Current was injected into $5\text{cm}^2$ hand electrode, and current return consisted of a metal plate covering the entire surface exposed when arm was sectioned from body. A pulsed source injected $10\text{ms}$ pulses having an amplitude of $4.5\text{kV}$ . . . . .	70
Figure 5.2	Diagram of injury model setup. Muscle tissue sample is exposed to a pulsed electric field generated by voltage source $V$ ( <i>Left</i> ). Cross-section of tissue sample between electrodes ( <i>Right</i> ) . . . . .	71
Figure 5.3	Conductance when considering intact and lysed cells. . . . .	71
Figure 5.4	Normalized conductivity fraction variation in biceps femoris of Sprague-Dawley rats as $10\text{ms}$ electric pulses are applied, for different electric field magnitudes. Data points calculated by applying (5.12) to experimental data reports by Bhatt <i>et al</i> [19] . . . . .	74
Figure 5.5	Normalized conductivity fraction variation as a function of number of pulses applied, obtained by fitting (5.4) to experimental data from [19] (data points marked with geometrical shapes in figure). Pointed lines show upper and lower 95% confidence bounds for the fitting. . . . .	75
Figure 5.6	Lised fraction $K_i$ as a function of muscle conductivity $\sigma_i$ , for the ranges used during the simulation. . . . .	77
Figure 5.7	Electric field magnitudes resulting from a $4.5\text{kV}$ shock. From left to right, each diagram shows the volumes inside the arm having increasing electric field strength. . . . .	78
Figure 5.8	Progressive damage (left to right) in muscle and tendon by cell lysis due to applied electric shock. . . . .	80
Figure 5.9	Progressive damage (left to right) in muscle and tendon by cell lysis due to applied electric shock. . . . .	81

# Chapter 1

## Introduction

### 1.1 Background

The most elegant solution for an electromagnetic problem is the exact mathematical solution. However, the complexity of closed-form solutions tends to grow faster than the complexity of the problem itself, making it extremely difficult to use analytical approaches as a general method. Closed-form formulations to complex electromagnetic problems can be unworkable for a variety of reasons, including difficulties handling complex solution regions, complexity in expressing boundary conditions of mixed types or boundary conditions that vary as a function of time, or having to account for anisotropic or inhomogeneous mediums [1]. We resort then to approximating the problem solution using systematic numerical treatments.

In this work, a numerical method to efficiently address a subset of electromagnetic problems, namely those dealing with large scale biological models that have relatively small detailed features and low frequency electromagnetic field interactions will be introduced.

Beyond first order approximations, electromagnetic problems involving biological bodies are complex. Biological bodies generally have complex geometries and large dimensions compared to the minimum feature size to resolve, its tissues are heterogeneous, and may present anisotropic dielectric properties. Moreover, if the models include metals embedded inside living tissue, it is sometimes necessary to account for electrochemical reactions, not unlike an electrode-electrolyte reaction inside a chemical battery [2]. Further, the dielectric properties of tissue, and hence the response to electromagnetic



stimuli may vary with tissue exposure history, field strength, frequency, current density, and temperature [3, 4]. A range of bioelectromagnetic interactions occur at low frequencies, as natural electric phenomena in cells, like neural activation, happen at frequencies ranges usually not higher than hundreds of cycles per second. Since the wavelength of signals at these low frequencies is much larger than the size of the entire model, the phase of the excitation signal can be considered constant across the entire problem space. In addition, the secondary magnetic fields caused by the currents inside the model are considered negligible. This approximation, known as the quasistatic approximation, is usually considered valid for frequencies up to tens of megahertz for models of the human body.

A general electromagnetic numerical method, appropriate to work well within all of these constraints, will be presented in Chapter 3; its use will be introduced in the context of two specific applications that cover a number of the issues that can be addressed using numerical bioelectromagnetic methods. These applications are calculations for an implanted retinal prosthesis to partially restore vision to people suffering from specific degenerative diseases of the eye, and modeling the effects of electric trauma on skeletal muscle tissue.

### 1.1.1 Retinal Prosthesis

Retinitis Pigmentosa and Age-related Macular Degeneration are degenerative diseases that disable a large percentage of photoreceptor cells, while leaving the rest of the visual neural path with a degree of functionality. Implantable retinal prostheses allow for partial restoration of some form of vision to patients blinded by photoreceptors loss; this is achieved by using of systematic electrical stimulation of the surviving ganglion and bipolar cells, replacing the functionality of the now damaged photoreceptor cells [5, 6]. There are multiple research efforts working on retinal implants [7, 8, 9, 10], and while different configurations have been devised, this dissertation will address the case in which an external camera and electronics capture and process a video signal, which is wirelessly transmitted to an intraocular implant, where the signal is delivered as electrical pulses to an epiretinal implanted electrode array, which, in time, excites the underlying retinal neural tissue.

The electrical stimuli provided by the implanted electrode array must have enough intensity to elicit visual percepts while at the same time be safe for prolonged human

use. As implantable electrode arrays become denser and smaller with the purpose of increasing resolution, more detailed anatomical models are needed to simulate electrical interaction between each electrode and the surrounding living tissue. To answer the question regarding what is the limit to miniaturize retinal electrode arrays, we need to look at the anatomy of the retina. Since neighboring cone and bipolar cells are interconnected, and each ganglion cell integrates the signal across the extent of its dendritic field, determining visual acuity in a healthy retina is not as simple as counting the density of rods and cones [11, 12]. Retinal cell density varies at different places in the retina, being greatest at the fovea, a specialized area of high resolution particularly sensitive to movement (early detection of movement is performed in the retina itself in mammals). Moving from fovea to periphery, ganglion cells show the greatest gradients in primates, decreasing in number, but having larger dendritic field size the farther apart from the center. Assuming the electrical stimulation takes place in the retinal ganglion cells, and an hexagonal packing of ganglion cells in the retina, the Nyquist limit is  $\lambda = \sqrt{3}a$ , where  $a$  is the spacing between neighboring ganglion cells and has a minimum value of  $2-3\mu m$ . For primate retinas,  $\lambda = 10\mu m$  [11]. This corresponds to about one minute of arc of the visual field. The normal eye's optic is diffraction-limited to filter out gratings with period length smaller than  $\lambda$ . The same eye optical imperfections that work as a spatial low-pass filter help spread a point stimulus to an average of 10 cones. This allows the retina to detect subtle lateral shifts in the image by comparing outputs of individual cones. It may be worth following this line of inquiry in future implanted devices, as at the same resolution, the ability to detect motion may vary drastically depending on the stimulation pattern used by the implant.

Currents and electric potentials induced in the retina by the implant are affected by a number of parameters of the implanted stimulator array, including electrode size, position of current return, and distance from the electrodes to the target stimulation area. All these parameters significantly influence the resulting charge injection. In Chapter 4, the multiresolution admittance method formulation introduced in Chapter 3 is used on different models of intraocular and extraocular retinal stimulation to determine electric potentials, current density magnitude, and possible retinal areas where neural activation could be achieved in the retina, using a numerical approximation of the activation function [13]. The human retina was modeled using a tissue-level layered model. This is a good approximation if we assume that the retinal structure beyond the photoreceptors is relatively healthy. However, it has been recently documented that retinal degenerative

diseases trigger remodeling of the neural structures of the retina [14, 15], particularly in advanced stages of the disease.

### 1.1.2 Electric Injury of Skeletal Muscle

It has been long known that the flow of large electric current through living tissue can cause trauma. The process that leads to tissue damage is complex. However, it is generally accepted that besides the thermal injuries caused by Joule heating [16, 17], lysis by cellular membrane electroporation [18, 19] and electroconformational denaturation of macromolecules (i.e. protein unfolding), affecting functioning of ionic channels in the cellular membrane are tissue-damage mechanisms [20, 19, 21, 22]. Effects of electric shock are frequency dependent [22]. While the cellular wall shields the cytoplasmic fluid from lower frequency components of the electrical current, at high frequencies the cell membrane is no longer an effective barrier to the passage of electrical current. Cell size, cell geometry, and solid-volume ratio also affect the outcome of applying supra-physiological electrical stimulation [17].

In Chapter 5, the multiresolution admittance method formulation introduced in Chapter 3 is used to numerically determine the electric injury effects of a high-voltage electric shock in skeletal muscle tissue of the human arm, including tissue impedance, currents across the arm, electric field distribution, and cellular damage expressed as percentage of lysed skeletal muscle cells.

## 1.2 Numerical Methods for Bioelectromagnetics

Many different numerical methods have been used for computing electric fields and current densities at low frequencies in bioelectromagnetic problems. Most of them use finite difference approximations, in which the problem is stated in terms of differential equations derived from Maxwell equations, and derivatives are approximated as finite differences between values at discrete points in the model. Some of the most used are:

1. Finite Difference Method (FD)
2. Finite-Difference Time-Domain method (FDTD)
3. Scalar Potential Finite Difference method (SPFD)

4. Impedance Method (IM)
5. Admittance Method (AM)

A brief discussion of each method's approach, strengths and weaknesses when used to treat bioelectromagnetic models follows.

### **Finite Difference method (FD)**

Originally introduced by Thom in 1928 as *the squaring method* [23], and widely used for modeling a variety of physical behaviors tractable using differential equations, the FD has been widely applied to solve electrostatic problems, by applying the Poisson and Laplace equations. The general idea behind the FD method is to solve differential equations by approximating them using a numerical finite difference equivalent, calculated by relating the dependent variable at the point considered to the values at neighboring points. The solution of a problem using the FD method involves three steps [1]:

1. Meshing the problem space into a grid defined by nodes.
2. Approximating the differential equation governing the problem by using the finite difference equivalent.
3. Solving the finite difference equivalent accounting for the boundary conditions.

While straightforward in theory, the application of FD method to bioelectromagnetic problems beyond electrostatics require numerical treatment that often depends on the particular problem, and results are frequently computationally more expensive than the alternative approaches.

### **Finite Difference Time Domain (FDTD) method**

The FDTD method was first described by Yee in 1966 [24]. In the original formulation, the problem space is subdivided using a regular grid, and a system formed by two dependent Maxwell equations (1.1) (1.2) is approximated using finite differences. These equations are iterated over time using two overlapped rectangular grids shifted half a cell in space. While originally the problem spaces considered were enclosed by perfect conductors, modern treatments manage free-space problems by including perfectly matched

layers (PML) positioned at the boundaries of the model space, preventing outgoing waves from reflecting back into the model [25, 26].

$$\frac{\partial \vec{B}}{\partial t} + \nabla \times \vec{E} = 0, \quad \vec{B} = \mu \vec{H} \quad (1.1)$$

$$\frac{\partial \vec{D}}{\partial t} - \nabla \times \vec{H} = J, \quad \vec{D} = \epsilon \vec{E} \quad (1.2)$$

The major restrictions to the use of the FDTD method for detailed large models and low frequencies are related to the stability criterion for the method (1.3).

$$\frac{1}{c} \sqrt{\Delta x^2 + \Delta y^2 + \Delta z^2} > \Delta t \quad (1.3)$$

In (1.3),  $c$  is the largest speed of light inside any material in the model,  $\Delta x$ ,  $\Delta y$ , and  $\Delta z$  are grid spacings in the  $\hat{x}$ ,  $\hat{y}$ , and  $\hat{z}$  direction respectively, and  $\Delta t$  is the time interval in between iterations. While conceptually simple, low-frequency simulations for large cell count models is usually computationally more expensive than SPFD and IM. The stability criterion imposes a hard boundary in the maximum  $\Delta t$  that can be used depending on the resolution of the model, making FDTD computationally expensive for high resolution models and low frequencies, both of which are requirements for our intended applications.

There are many variations and optimizations for the FDTD method, including quasi-static formulations appropriate for low-frequencies that consider decoupled static electric and magnetic fields under certain conditions [27, 28]; these treatments are, however, tailored to solutions of specific problems and computationally more expensive than alternative methods as SPFD and IM.

### Scalar potential finite difference (SPFD) method

The SPFD method was introduced by Dawson *et al* in 1996 [29, 30], and is a quasistatic scalar method, derived from incorporating the influence of an applied magnetic field as a vector potential in the electric field. Starting from the differential expression of the Maxwell-Faraday equation in frequency domain (1.4), the magnetic field  $\vec{B}$  can be expressed in terms of a magnetic vector potential  $\vec{A}$  as (1.5).

$$\nabla \times \vec{E} = -\frac{\partial \vec{B}}{\partial t} \quad (1.4)$$

$$\nabla \times \left( \vec{E} + \frac{\partial \vec{A}}{\partial t} \right) = 0 \quad (1.5)$$

$$\vec{E} = -\nabla V \quad (1.6)$$

If no free charges are initially present in the solution space, and considering (1.5) and (1.6),  $\vec{E}$  can be written as indicated in (1.7).

$$\vec{E} = -\nabla V - \frac{\partial \vec{A}}{\partial t} \quad (1.7)$$

Substituting  $\vec{E}$  from (1.7) into Gauss' Law (1.8) results in (1.9), the scalar treatment that is used for SPFD. A FD technique is then used to solve the system based on potentials of neighbor cells and conductivities.

$$\nabla \cdot (\sigma \vec{E}) = 0 \quad (1.8)$$

$$\nabla \cdot (\sigma \nabla V) = \nabla \cdot \left( -\frac{\partial \vec{A}}{\partial t} \right) \quad (1.9)$$

SPFD can readily be used to determine electric potentials and current density magnitudes in the problem space. In addition, because it is a strictly scalar method, it is computationally less expensive than the IM and AM [31]. The multiresolution method introduced in Chapter 3 allows for efficient processing of large-scale models, and can in principle be used with SPFD as well as other numerical methods including AM and IM. At difference than the AM and IM, the SPFD method does not imply an intermediate representation of the problem space in terms of an electric network. This takes away the ability to augment the model by using lumped elements to approximate electrochemical or bioelectrical effects such as electrode-metal interfaces [32] or cellular membrane bioelectrical behavior [33].

## Admittance Method (AM) and Impedance Method (IM)

The AM was introduced by Armitage in 1983 [34]. Shortly after, in 1984, Gandhi described a complementary method, the IM [35]. While the AM and the IM numerical treatments are slightly different, both methods are equivalent in approach, capabilities, and results. This dissertation will generally refer to an admittance formulation, but the discussion applies to both methods. As with SPFD, both AM and IM assume a quasi-static approximation in which the secondary magnetic field caused by currents inside the problem space is considered negligible. If a magnetic field is used for stimulation, an additional assumption is made, namely that the incident magnetic field is not disturbed by the materials in the model.

The general procedure for the admittance method involves partitioning a problem space into smaller domains considered homogeneous, from which an equivalent impedance network is derived. Each domain has a known conductivity value. While there is no restriction regarding how the problem space is partitioned, in practice, using Cartesian orthogonal directions helps make the implementation easier. While the impedance or admittance matrix is consistently obtained from the dielectric properties of the underlying materials and tissues, the numerical treatment is highly dependent on the stimulation method used. When using magnetic fields to inject power, the system is set up by applying Kirchoff Voltage Law, an impedance matrix is used, and the solution yields the edge branch currents. When using current sources, the system is obtained by applying Kirchoff Current Law, an admittance matrix is used, and the solution yields the node voltages.

Taking as an example the common case of a three dimensional model regularly partitioned as cuboid voxels using Cartesian coordinates, the equivalent admittance value for each of the edges of voxel  $(i, j, k)$  along the  $\hat{x}$  direction,  $g_x^{i,j,k}$ , is approximated by (1.10).

$$g_x^{i,j,k} = \sigma_x^{i,j,k} \frac{\Delta y \Delta z}{\Delta x} \quad (1.10)$$

In (1.10),  $\Delta x$ ,  $\Delta y$ , and  $\Delta z$  are the lengths of the edges in the  $\hat{x}$ ,  $\hat{y}$ , and  $\hat{z}$  directions respectively. The resulting electric network is expressed as an admittance matrix, and a system having the form (1.11) is created.

$$G V = I \quad (1.11)$$

In (1.11),  $G$  is the admittance matrix,  $V$  is the voltage vector, and  $I$  is the current vector. External stimulation is applied, often by means of a time-varying magnetic field [34] or a continuous or sinusoidal ideal current source [36], and introduced in the numerical formulation (1.11) in terms of the appropriate values in vectors  $V$  or  $I$ .

The linear system is solved, and the unknown scalar variable  $V$  or  $I$  obtained. Electric field can be reconstructed from mesh geometry and scalar potential. Literature discusses impedance method solutions in which static [37, 36] or frequency domain [35, 34, 38] formulations are both addressed. In addition to these cases, a time-stepping transient numerical solution is introduced in Chapter 3.

A distinctive advantage of the impedance and admittance methods is that since they include an intermediate step in which the model is represented as an electrical network, new electrical components can be arbitrarily included in the circuit to account for electromagnetic effects not captured by the original model. This feature is valuable to model complex bioelectrical behaviors, such as electrode-electrolyte interfaces between implanted electrodes and neural tissue, which are often described in terms of circuitual lumped elements [32].

### 1.3 Organization of Dissertation

This dissertation introduces an efficient numerical treatment generic enough to be useful for a variety of low frequency bioelectromagnetics problems, and presents examples of its use in the context of two applications: retinal implants and the determination of electroporation damage in skeletal muscles due to a high-voltage electric shock. A brief introduction to the applications, as well as a short description of methods adequate for numerical low-frequency numerical treatments of bioelectromagnetic problems was introduced in this chapter. Chapter 2 reviews applications of the admittance method to problems involving biological bodies, and briefly develops background concepts and techniques that will be required for Chapter 4 and Chapter 5. Chapter 3 introduces a formulation of a multiresolution variant of the admittance method suitable for analysis of large computational models and biological bodies. Chapter 4 provides examples of applications of the multiresolution admittance method to medical implantable devices, focusing on the retinal prosthesis to restore partial vision to the blind. Chapter 5 introduces applications of the multiresolution admittance method to model injury by cellular



lysis caused by a high voltage electric shock. Finally, Chapter 6 presents conclusions.

## Chapter 2

# The Admittance Method in Bioelectromagnetic Problems

### 2.1 Introduction

Early on, most bioelectromagnetic applications of the admittance and impedance method involved determining the effects of exposure to external electric or magnetic fields, with interest focused on calculating the energy absorbed by tissue [34, 39, 35]. The models contemplated biological tissues and air, and usually did not include metallic parts. More recently, with the advent of electrically powered medical implants and advanced medical imaging technologies based on electromagnetic fields, a host of new bioelectromagnetic problems presenting unique challenges have arisen. Research focus has shifted towards interdisciplinary efforts, in which not only the direct effects of electromagnetic fields, such as power deposited, are determined, but also the biological responses, like the cell recruitment volume [40], tissue impedance change [19], effects of electromagnetic stimulation in eliciting responses from the nervous system [41, 37], and trauma caused to living cells [42] are taken into account.

While modeling the human body with a relatively coarse resolution is often appropriate for dosimetry purposes, these new problems often require high level of detail in anatomically correct models over large volumes. This significantly increases the processing time and memory requirements. Further, the incorporation of metallic parts and dielectrics inside living tissue, results in complex electrochemical interactions between metal and electrolytes that add complexity to the treatment.

In the following sections, a brief survey of applications of the admittance method to bioelectromagnetic problems is presented, along with background information about specific issues related to modeling bioelectromagnetic problems using the admittance method.

## 2.2 The Admittance Method for Bioelectromagnetic Problems

We will now briefly discuss some of the most common applications and formulations of the impedance and admittance method in chronological order. The first reported description dates from 1983 [34], when Armitage introduced the admittance method, which is equivalent to the impedance methods in terms of approach and results, but formulated in terms of admittances. In his 1983 paper, Armitage calculated the instantaneous specific absorption rate (SAR) distribution inside a model of the human body when exposed to radiofrequency (RF) electromagnetic waves. His model of the human body was derived from CT scans, used a three dimensional grid with internode spacings of 0.5 *cm* to 2 *cm* for different runs, and described the human torso in terms of seven tissues. Capacitive electrodes and inductive coils were considered as the possible applicators. A body phantom filled with an agar-based medium was used to experimentally verify the resulting temperature increase predicted by the simulations. As for the formulation, it used frequency domain description assuming a single frequency. Instantaneous SAR was calculated as indicated in (2.1).

$$SAR = \frac{P}{D} = \frac{|\vec{E}|^2}{D} \sigma \quad (2.1)$$

In (2.1),  $P$  is the instantaneous power dissipated per unit volume,  $D$  is the mass density of the material,  $\sigma$  is the conductivity of the material, and  $\vec{E}$  is the instantaneous electric field obtained from the electric potential  $V$  and the magnetic vector potential  $\vec{A}$  as

$$\vec{E} = -\nabla V - \frac{\partial \vec{A}}{\partial t} \quad (2.2)$$

In (2.2), the term  $\frac{\partial \vec{A}}{\partial t}$  accounts for the magnetically induced electric fields inside the

model and is only considered in the case where inductive coils are used for stimulation. The body tissue was modeled as a grid of cuboid cells, each interconnected at its vertices with its neighbors; tissue conductivities are represented using admittance lumped elements instead of impedances, and each admittance element has an associated voltage source in series to account for the induced electric fields when using magnetic stimulation. The voltage sources are not needed when the energy is delivered using the capacitive applicators. Armitage used successive overrelaxation (SOR) to solve the network. In order to use the capacitive electrodes as voltage sources in the model, boundary conditions were enforced by setting the voltages of the nodes attached to the electrodes to the desired stimulation voltages, and having these nodes omitted from the iterations when solving the linear system.

In 1984, Gandhi introduced a new formulation, this time using impedances to analyze the power deposition in tissues in hyperthermia [35]. The frequencies considered were 13.56 MHz and 27.12 MHz. The model contemplated two-dimensional slices of a human torso obtained by scanning anatomic diagrams, having a resolution of  $25 \times 32$  cells. In this particular application, it was noted that the impedance network converged much faster than the equivalent finite difference approximation. In Gandhi's formulation, tissue conductivities are used to derive an equivalent lumped-element impedance network, and power is introduced in the model by a harmonic homogeneous or spatially varying magnetic field, which drive electromotive forces (EMF) in the impedance loops in the model. The induced EMFs are calculated using Faraday's law, and used to formulate a linear system along with the impedance matrix. As in Armitage's paper, the resulting system is solved for branch currents using SOR. The SAR is subsequently calculated using a finite difference approximation of the gradient of the electric potential obtained from the impedance method solution. The precision of the method is verified against the analytical solution for a similar problem using infinitely long concentric cylinders.

In 1985, Deford, a student of Gandhi, published an article in which in addition to the two-dimensional slices of a realistic human torso, a three-dimensional cuboid model is used to coarsely approximate a human body. The cuboid had the proportions of a man standing in anatomical neutral position, was meshed to 9800 cells using an expanding grid algorithm, and considered muscle, fat, and a thin skin layer at its surface [39]. Other than the model, the formulation and verification are identical to Gandhi's original paper [35]. Deford noted in his article that the run time of the simulations was extremely fast when using the impedance method compared to solving the same problem using the

method of moments. In 1988, Orcutt used the impedance method to predict the power absorbed by the human body when exposed to a nuclear magnetic resonance imaging device [43]. As in Gandhi's and Deford work, an impedance network was formed and transformed to a linear system by describing Kirchoff voltage equations for a sufficient number of planar loops in the network. The model used was the most sophisticated to date, consisting of a complete three-dimensional human body meshed using cubic voxels having 1.31 *cm* per side, and considering 15 different body tissues. The excitation used was a 30 *MHz* magnetic field, polarized front to back of the model. The method was verified against the analytical solution for a sphere having the dielectric properties of muscle subjected to an external magnetic field.

In 2003, Eberdt presented a formulation that contemplated a two-dimensional multi-resolution meshing algorithm and its extension to three-dimensions [36]. Eberdt briefly discussed applications of the new meshing algorithm for very detailed anatomical structures. The same year, Nadeem used the impedance method for modeling electroconvulsive therapy (ECT) and transcranial magnetic stimulation (TMS) devices [44]. Nadeem's model was based on the head of the male dataset from the Visible Human project [45].

## 2.3 Modeling the Human Body with the Admittance Method

For human anatomical models with resolution in the order of millimeters or more, full male and female data sets are available, including the ones from National Library of Medicine [45]. Models at these resolutions can be developed using modern medical imaging techniques such as magnetic resonance. For higher resolution models, the model data can be either interpolated from coarser datasets or computer generated. Models used through this dissertation take were made using interpolation techniques to increase spatial resolution, as well as computer generated models from geometrical anatomical descriptions. In some of the applications presented in later chapters, both methods have been merged using the geometrical models for the areas of fine detail and the interpolated models for the bulk of the tissue, to establish adequate boundary conditions for the simulations.

A discrete model made of cubic voxels can be generated from an anatomical geometric description by periodically sampling the model space at the maximum resolution to be

used. A homogeneous cubic voxel is considered around each sampled point. Each voxel is characterized using a material index, and treated as a volume having homogeneous electrical properties. One material index, usually number zero, is reserved for void volumes; this allows for arbitrary culling of voxels in well known areas for performance purposes (i.e. inside a perfect conductor), as the voxels assigned with material index zero are not represented in the equivalent admittance network, and are assigned an arbitrary value for the scalar electric potential during post-processing.

The presence of complex surfaces and fine structures intermingled with larger, homogeneous areas is characteristic of biological tissue. Compounding this, for certain applications like the modeling of implanted devices, the size of the model tends to be large compared to the anatomical details close to the area of interest. Using efficient multiresolution meshing techniques, capable of adapting to preserve detail in the areas of interest and reduce detail elsewhere is important to create realistic models that can be processed using reasonable computational resources.

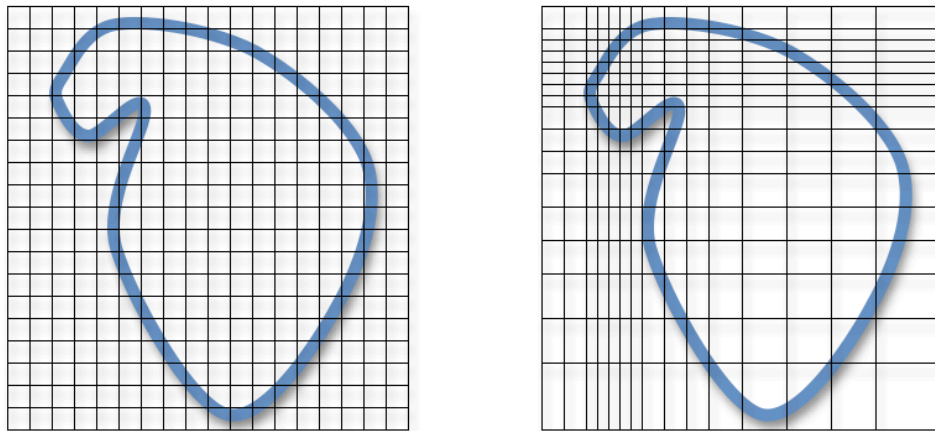


Figure 2.1: Two-dimensional uniform meshing (*Left*), and expanding grid meshing (*Right*). Note the higher resolution at the top left of the expanding grid plot. The expanding grid is more efficient in terms of computational resources, as it allows finer resolutions in parts of the problem space at the expense of less precise results in other portions of the model.

When using the admittance method, the problem space needs first to be discretely partitioned; while any geometric space partition is acceptable in theory, in practice is con-

venient if the partitioned model is represented in terms of a three-dimensional orthogonal mesh or, equivalently, as a collection of voxels. In previous works, the meshing grid was considered to be of uniform resolution [35][44], two-dimensional [36], or expanding [34]. Two-dimensional examples of uniform and expanding meshing grids are shown in Figure 2.1. Each of these approaches have advantages and drawbacks. For three-dimensional models, assuming same unit voxel size for each method, uniform resolution meshes provides the most accurate results at a price of greatly increasing the required computational resources used. Two-dimensional models are not always adequate for modeling complex three-dimensional problems, but can provide a good approximation for certain symmetric geometries using minimum resources. Expanding grids, while easy to implement, are suboptimal because they tend to be highly non-local; an increase in the resolution of a small part of the model increases the resolution on distant parts as well and, because of this, if the problem requires multiple high-resolution sub-volumes, this quickly escalates the computational resources needed. In addition, when using expanding grids, the error of the numerical solution is larger in the portions of coarser resolution.

The alternative multiresolution meshing approach introduced in Chapter 3 creates compact three-dimensional meshes for large models, consumes a small fraction of the computational resources of the uniform resolution equivalent mesh, and allows for selective increase of resolution in any number of desired sub-volumes. The algorithms for meshing and network generation presented are inherently local; writing a parallel computing implementation is trivial. The introduced formulation allows for resource-efficient computation of large, complex, three-dimensional models and the use of arbitrary stimulation waveforms using time-stepping.

# Chapter 3

## A Three-Dimensional, Time-Stepping, Multi-resolution Admittance Method

### 3.1 Introduction

The basic procedure for the admittance method in three dimensions involves partitioning a problem space into cuboid shaped voxels considered homogeneous. An equivalent admittance network is then derived by placing network nodes on the vertexes of each voxel, and lumped admittances along its edges. The equivalent lumped admittance value for each edge is calculated from the averaged conductivity of the voxels that share that edge. External stimulation is applied by means of a time-varying magnetic field [34] or an ideal current source [36]. The resulting network is then solved for the voltage of each node. Literature discusses impedance and admittance method solutions in which static [37, 36] and frequency domain [35, 34, 31, 46, 38] formulations are presented. The lumped element circuit approximation used is valid only under a quasistatic approximation: the size of the model must be small compared to the wavelength of the excitation signal. In addition, the secondary magnetic field caused by the currents flowing through the network is considered negligible. While the quasistatic approximation prevents the method from modeling electromagnetic wave propagation, it is a good approximation for low frequency problems.

The admittance method variant introduced in the following sections presents two



significant new features respect to the methods described in literature: First, a multi-resolution three-dimensional meshing algorithm that creates compact meshes without significantly increasing error is introduced. Secondly, a time-stepping formulation is used to calculate transient behavior of models stimulated by arbitrary waveforms.

The steps for preparing and running a simulation using this multiresolution admittance method treatment include discretization, multiresolution clustering, equivalent network generation, network solving, and post-processing. Each of these steps is addressed in order in the sections of this chapter.

### 3.1.1 Modeling and Discretization

To apply the multiresolution admittance method, a discrete model of the system to simulate is required. The model must include geometry, electrical conductivity of each material considered in the model, and a description of excitation sources.

#### Discretization

Each material present in the model to simulate is first assigned a unique *material index*. Each material index has a conductivity value associated to it. The geometry of the model is encoded by using a three-dimensional array and having each element of the array representing a single cubic voxel and tagged using the appropriate material index. Each of these cubic voxels will be referred hereafter as a *unit voxel*. Unit voxels are considered homogeneous, but the constitutive material can be anisotropic. The edges of each voxel are parallel to the  $\hat{x}$ ,  $\hat{y}$ , and  $\hat{z}$  directions of the Cartesian coordinate grid.

While there is no mathematical constraint that requires the partition of the space to be in terms of cuboid voxels or to use a Cartesian coordinate grid, having a regular, orthogonal decomposition of space is helpful to simplify the calculation of the associated network later on. The size of the array is given by the maximum resolution of our model. For instance, if the model describes a cubic portion of space of 6.4 cm per side at 1 mm resolution, the discrete model will have  $64 \times 64 \times 64$  voxels; the three-dimensional array used to encode this model will have the same number of elements.

## Frequency Dispersion Considerations

While the impedance method as described here does not directly account for frequency dispersion, the following approaches can be used if the dielectric properties of the materials in our model vary significantly with frequency. First, if most of the power in the excitation waveform is confined to a narrow frequency range, frequency domain analysis for the excitation waveform can be performed and the dielectric properties for each material in the model can be chosen close to the value of the maximum frequency component; this is compatible with time-stepping transient solving. Second, if the excitation waveform peaks at multiple frequency values, the system can be solved one time for each peak present in the frequency domain, and the single-frequency results combined using the superposition property of linear networks to obtain the final numerical results.

### 3.1.2 Multiresolution Clustering

Multiresolution meshing refers to the generation and use of a model in which space has been divided into smaller sub-volumes (voxels) of different size, with the goal of saving computational resources. While straightforward methods have been described for two-dimensional models [36], their complexity increases substantially when attempting to implement them in a three-dimensional space. Because of this, a different approach was chosen. Instead of partitioning a large model into differently sized voxels, the volume is first finely subdivided into voxels of the smallest size considered and then a multiresolution clustering algorithm is used to coarsen the resolution by selectively aggregating neighbor voxels as shown in Figure 3.1.

Multiresolution clustering reduces the model's voxel count by aggregating neighboring voxels into larger voxels, keeping spatial resolution high in the areas close to material boundaries, and progressively increasing the size of voxels at more homogeneous parts of the model. The proposed algorithm is local, in the sense that voxels that are close to each other are processed together, making a parallel computing implementation easy to accomplish. The multiresolution schema works independently of the geometry of the model.

The size of the model in all three dimensions must be powers of two. This does not prevent us from using arbitrary model sizes, as the restriction can be fulfilled by temporarily growing the dimensions as needed using voxels tagged with a specific material number, so they can be stripped out after multiresolution clustering process has

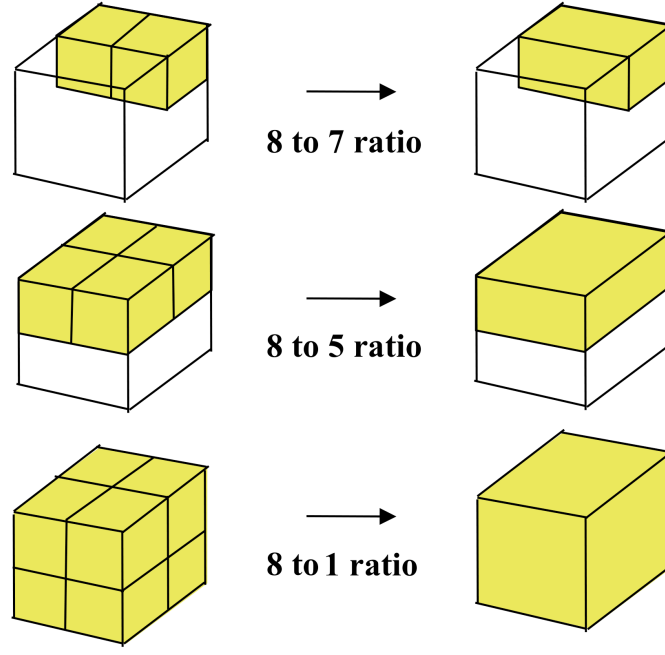


Figure 3.1: Applying the multiresolution clustering algorithm results in the normalized cases above. The voxel reduction ratio obtained during multiresolution clustering varies depending on model geometry and other constraints described in the Clustering Constraints section. Note how vertices are discarded during the clustering process, leading to a reduced number of node equations in the equivalent electrical network.

completed.

A convention is adopted in which a voxel position is given by the coordinates of its lower left back vertex. This way, a cubic voxel having sides of size one, with all faces parallel to planes normal to the coordinate axes, and having a vertex at the point  $(x = 0, y = 0, z = 0)$  and the diagonally opposite vertex at  $(x = 1, y = 1, z = 1)$  will be said to have a position  $(0, 0, 0)$ .

### Clustering Constraints

The multiresolution clustering algorithm presented here keeps the size of the voxels next to material boundaries at the unit size and progressively increases the size of voxels inside larger homogeneous volumes in the model. While this approach is in general appropriate, there are some cases in which further control of the clustering process is required. To address this need, three types of geometric constraints are considered when clustering:

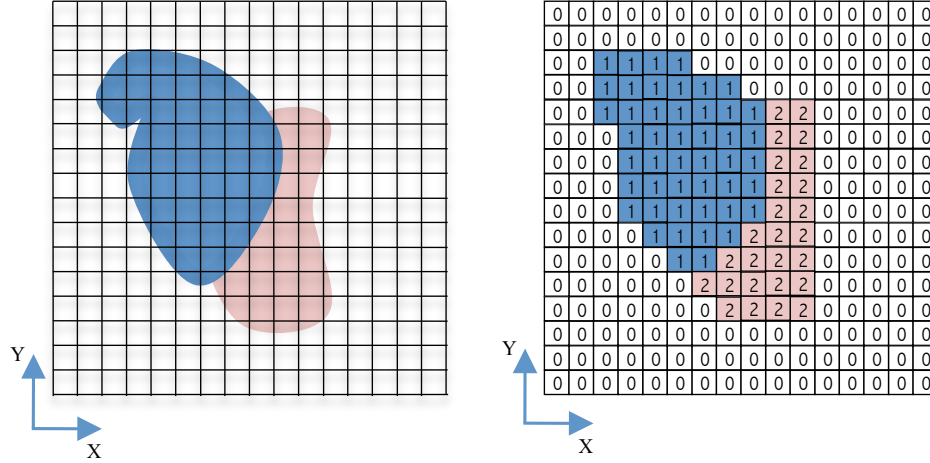


Figure 3.2: Discretization procedure, using a 16 x 16 x 1 unit voxel grid for illustration purposes. Three materials are considered in this example, tagged as 0, 1, and 2 respectively. Note that a real model would have to further extend in the  $\hat{z}$  direction to properly account for boundary conditions. Starting from a representation of the model (left), a regular cubic mesh is overlaid, and the center points of each voxel are sampled. Voxels are then considered homogeneous, and different numbers are assigned to each material (right). Dielectric properties are associated to the material number.

*named nodes, sub-volumes, and guide points.*

Named nodes are nodes that are guaranteed to appear in the final mesh. Since the clustering algorithm removes nodes when adjoining voxels, as shown in Figure 3.1, named nodes are used to ensure certain important nodes, as for instance the ground node, or a current injection node, are not removed.

A sub-volume is a cuboid-shaped space partition inside the model in which a maximum voxel size is defined. The purpose of defining a sub-volume is to preserve high spatial resolution inside that portion of the model during multiresolution clustering. Sub-volumes are defined by specifying their location, size, and the maximum voxel size allowed inside them.

A guide point is a rule that when applied to a point in the model, defines a constraint on the voxel size of all the voxels as a function of a distance to the point. Guide points are useful in cases where power is injected into the model at a single node, to help gradually coarsen the resolution of the voxels while achieving a smooth current distribution. The size versus distance function can be arbitrary; a polynomial function (3.2) has been used

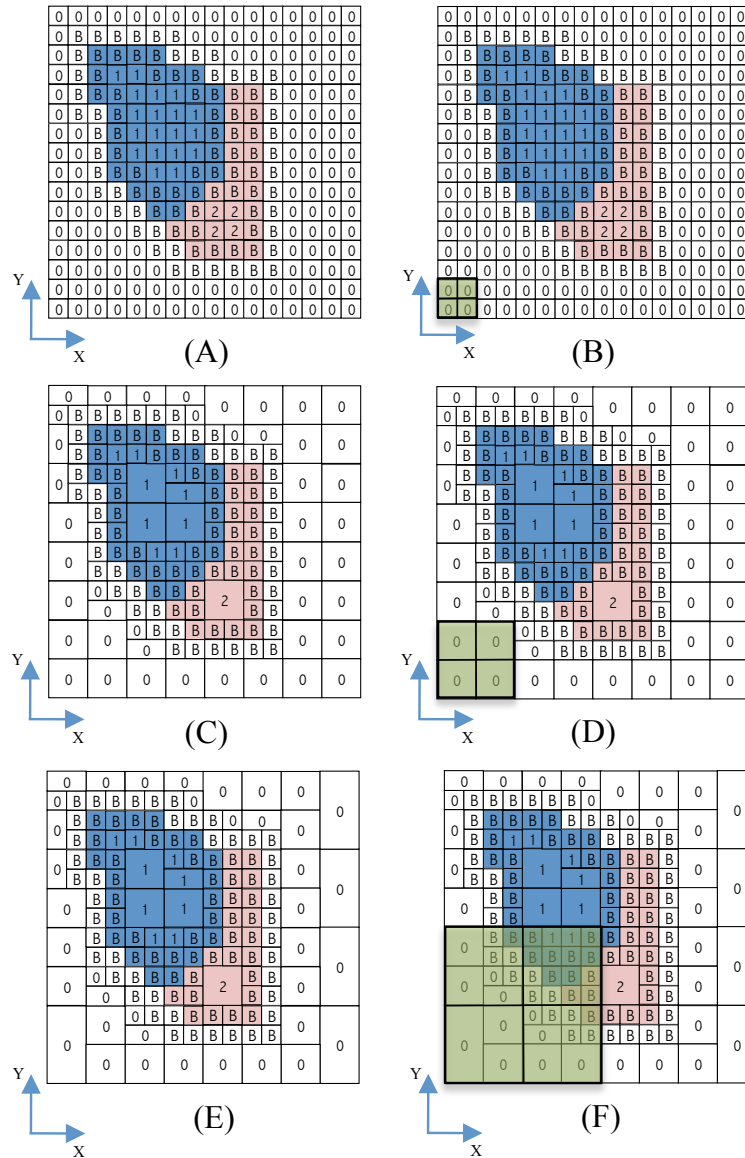


Figure 3.3: Multi-resolution clustering. Starting from the model of Figure 3.2, boundary voxels are marked using a 'B' character.(A), and a quadrant (octant, if in 3D) of size  $S = 2$  is swept through the span of the model (B), clustering voxels inside it that are made of the same material, are not boundaries, and comply with the clustering constraints described in the text (C). Clustering order in this example was first along  $\hat{x}$  and then along  $\hat{y}$ . The size of the quadrant is doubled (D), and the operation is repeated (E). When no more clustering is possible, the process is complete (F). Result is as shown in Figure 3.4.

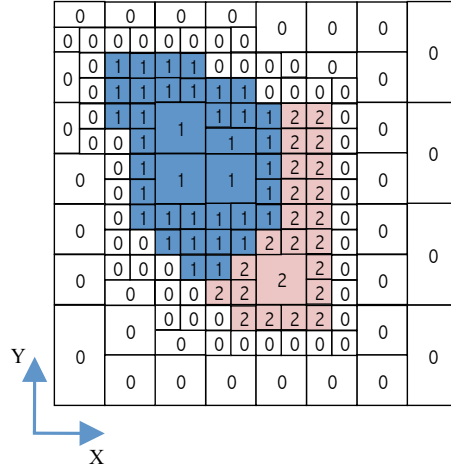


Figure 3.4: Result after processing the model presented in Figure 3.2 using the multi-resolution algorithm. The voxel count has been reduced by 55% compared to the uniformly meshed model. In larger realistic biological models, voxel count reductions on the order of 80 percent are not uncommon.

for the different applications presented in Chapter 4 and Chapter 5. In (3.1),  $(x, y, z)$  is the position of the guide point, and  $d$  is the distance from the current voxel position  $(i, j, k)$ . In (3.2), the two coefficients  $a$  and  $b$  define the maximum allowable voxel size  $s$  for the voxel at  $(i, j, k)$ . The effect of using guide points can be observed in Figure 3.5. Multiple named nodes, sub-volumes, and guide points can be defined for a model to constrain the maximum allowable sizes of each and every voxel in the model. A cross section for a resulting multi-resolution mesh of a concentric solid sphere and spherical shell obtained using this algorithm is shown in Figure 3.5

$$d = \sqrt{(x - i)^2 + (y - j)^2 + (z - k)^2} \quad (3.1)$$

$$s = \lfloor ad + bd^2 \rfloor \quad (3.2)$$

### Three-dimensional Multi-resolution Clustering Algorithm

The algorithm to create a multi-resolution mesh from a uniform mesh by clustering contiguous voxels may be described as follow:

## 1. Initialization:

- (a) If the model array size along any of the orthogonal axes is not a power of 2, grow the array in that dimension up to a size that is power of 2, tagging the newly added voxels with material= *void*.
- (b) Sweep entire model array, marking voxels belonging to a material boundary, that is, with its sides, edges or vertices in contact with a voxels of different material, as *boundary voxels* (shown in Figure 3.3-A).
- (c) Mark voxels at each named node as a boundary voxels. At least two named nodes are always defined: one for the node that will be the electrical ground, and one for each node in which a current is being injected into the model. This guarantees that these nodes exist in the final model.
- (d) Initialize variable  $S = 2$ .  $S$  represents the size of the side of the volume space we are considering cluster in this iteration.
- (e) Initialize constant  $M$  to the maximum allowable size given in terms of unit voxels for any voxel in the model.  $M$  must be a power of 2. For instance, setting  $M = 16$  indicates that after clustering, the maximum size allowed for any multiresolution voxel in the model is 16 unit voxels per side.
- (f) (optional) One or more sub-volumes are defined by specifying size, position, and maximum allowable voxel size inside their volume.
- (g) (optional) One or more guide points are defined by specifying their position and their  $a$  and  $b$  coefficients.

## 2. Recursive Clustering:

- (a) Initialize  $i = \frac{S}{2}$ ,  $j = \frac{S}{2}$ , and  $k = \frac{S}{2}$
- (b) Consider a cubic volume centered at  $(i, j, k)$ , and having a side size of  $S$  unit voxels. This volume can be sub-divided in eight octants, all of which share the point  $(i, j, k)$ .
- (c) Any two voxels  $A$  and  $B$  inside the cubic volume considered in (a) can be joined into a single voxel  $C$  if they comply with the all the following constraints:
  - i.  $A$  and  $B$  span one (or more) entire octant(s) of the sub-volume each.
  - ii. Both  $A$  and  $B$  are tagged with the same material index.

- iii.  $A$  and  $B$  share a common face.
  - iv. Neither  $A$  or  $B$  are marked as a boundary voxel.
  - v. Neither  $A$  or  $B$  share a vertex with any voxel whose smallest sized side is smaller than the smallest side of  $A$  or  $B$ .
  - vi. The largest dimension of the voxel created by adjoining  $A$  and  $B$  along any coordinate axis is less than or equal to any restriction in dimension specified at the origin point of the new voxel by  $M$ , a sub-volume definition, or a guide point restriction.
- (d) If step 2.(c) resulted in a join operation, apply step 2.(c) again. If not, continue with step 2.(e) below. All the possible outcomes of step 2.(c) are shown in Figure 3.1.
- (e) A new position is calculated by incrementing either  $i$ ,  $j$ , or  $k$  by a value of  $S$ . The order of increment is not important, but the entire volume of the model must be covered. If the entire model has been traversed, continue with step 3 below. Otherwise repeat steps from 2.(b).
3. If at least one clustering operation has occurred at step 2, double the value of  $S$  and repeat step 2.
4. Remove all voxels tagged as material=*void*. Exit.

## Two-dimensional Multi-resolution Clustering

The three-dimensional multiresolution clustering algorithm described in the previous section can be applied to two-dimensional grids by reducing the number of dimensions in the geometry by one degree, that is, by considering only two coordinate axis instead of three, quadrants instead of octants, and voxel edges instead of voxel faces.

Figures 3.2, 3.3 and 3.4 illustrate a sample case in which two-dimensional multi-resolution clustering is used.

### 3.1.3 Electric Network Generation

We will now to derive the topology of a lumped circuit element that is an approximate electrical description of a single voxel in the model, and obtain the expressions to calculate



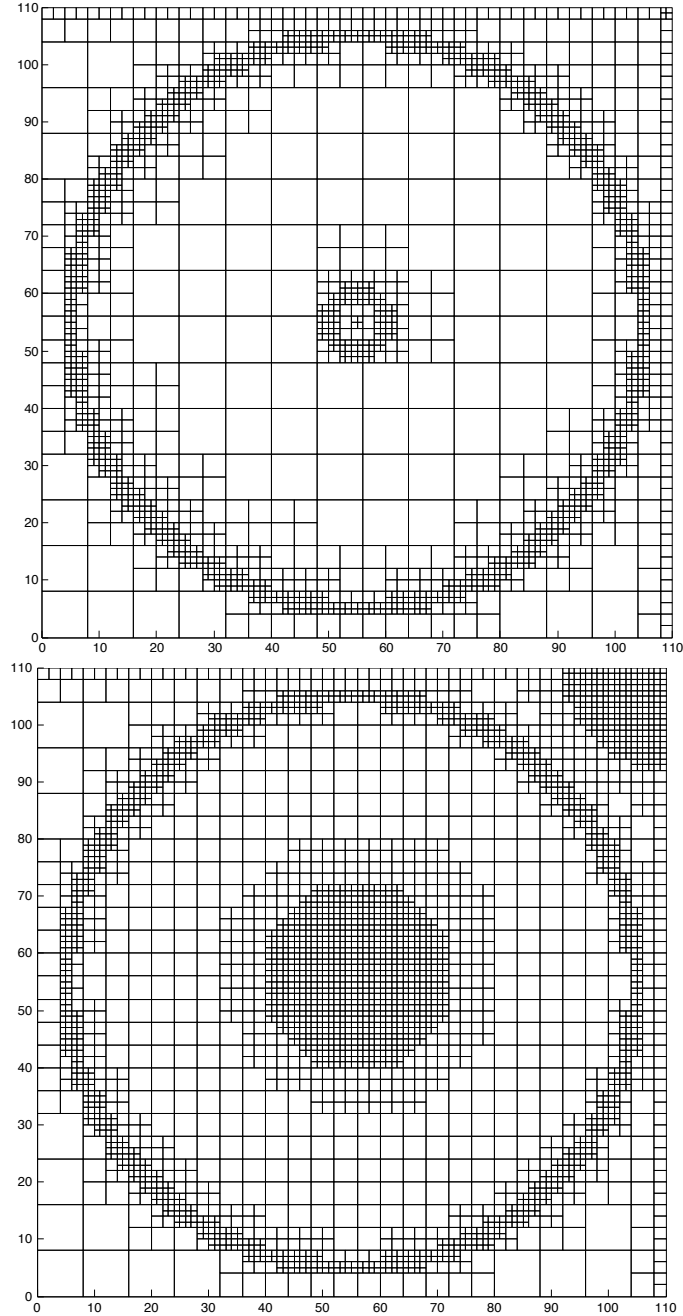


Figure 3.5: Transversal slices of multiresolution mesh of a model of a spherical capacitor. The top plot corresponds to a multiresolution mesh having a maximum voxel size of  $M = 8$ . The bottom plot is the same case with the addition of two guide points at the terminals of the device, at the center and upper left of the Figure respectively, defined using (3.2) with  $a = 0.12$  and  $b = 0$ . It can be observed how the mesh gradually coarsens from the guide points. This has the effect of creating a smooth spread of the injected current, lowering the numerical error.

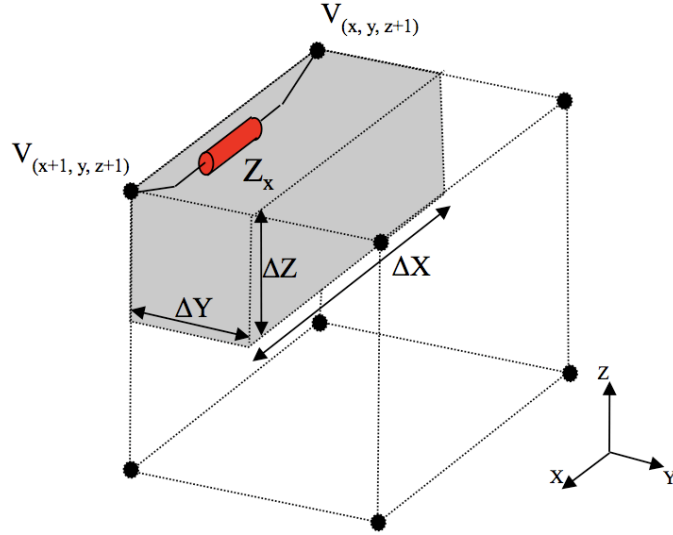


Figure 3.6: Equivalent circuit network topology. Network nodes are congruent with the vertices of each voxel, and network impedances are connected between nodes along each of the edges of each voxel. Each edge impedance accounts for modeling a quarter of the voxel's volume in one direction. If one edge is shared among two or more voxels, the edge impedances for each participating voxel are combined in parallel, effectively averaging dielectric properties for all voxels involved.

the different circuit components involved. In order to maintain a good spatial correlation between the electric equivalent network and the original model, the circuit nodes are placed in the vertices of each voxel. Since vertices are connected by edges, the lumped circuit elements that will represent our model will be placed along the edges of the voxels. This has the added advantage of performing an orthogonal decomposition of the currents and fields, which will simplify vector reconstruction and will allow to use linearity to determine the whole voxel equivalent circuit.

$$\vec{J} = \sigma \vec{E} \quad (3.3)$$

As illustrated in Figure 3.6, each edge impedance represents one quarter of a voxel in a given direction. To determine the topology of the equivalent circuit for each edge, we start from Ohm's Law expressed as (3.3), where  $\vec{J}$  denotes the current density vector,  $\sigma$  the complex conductivity, and  $\vec{E}$  the electric field. Note that in the more general case of anisotropic material, the conductivity  $\sigma$  can be represented as a second rank tensor. Considering only the components in the  $\hat{x}$  direction, and frequency domain, the complex

conductivity of the material along  $\hat{x}$  can be expressed as a function of an impedance (3.4), where  $J_x$  and  $E_x$  are respectively the current density and electric field components in the  $\hat{x}$  direction,  $Z_x$  is the equivalent edge impedance in the  $\hat{x}$  direction for a volume spanning a quarter of the voxel, having a cross section of  $(\Delta y \Delta z)$  and a thickness of  $\Delta x$ , as illustrated in Figure 3.6.

$$\begin{aligned} (\sigma_x + j\omega\epsilon_x) &= \frac{\mathbf{J}_x}{\mathbf{E}_x} \\ &= \frac{1}{Z_x} \frac{\Delta x}{\Delta y \Delta z} \end{aligned} \quad (3.4)$$

Rearranging (3.4), the equivalent impedance for the edge can be written as (3.5) .

$$\begin{aligned} Z_x &= \frac{1}{(\sigma_x + j\omega\epsilon_x)} \frac{\Delta x}{\Delta y \Delta z} \\ &= \left( \sigma_x \frac{\Delta y \Delta z}{\Delta x} + j\omega\epsilon \frac{\Delta y \Delta z}{\Delta x} \right)^{-1} \end{aligned} \quad (3.5)$$

$$Z_x = (\text{Admittance} + \text{Susceptance})^{-1} \quad (3.6)$$

From (3.5) we can see that the expression is of the type (3.6), describing the parallel circuit of a resistor with a capacitor for the impedance associated with the edge. Having each edge of each voxel accounting for the impedance of a quarter of the voxel in a given direction, and using superposition property to overlap all three orthogonal coordinate directions, we obtain the configuration shown in Figure 3.7.

The lumped element values for the resistor and capacitor for the edge impedance depicted in Figure 3.6 can be calculated as shown in (3.7) and (3.8). When multiple voxels share common nodes, there will be more than one edge running between two nodes; this will be taken into account later by considering them in parallel when building the impedance matrix to solve the linear system.

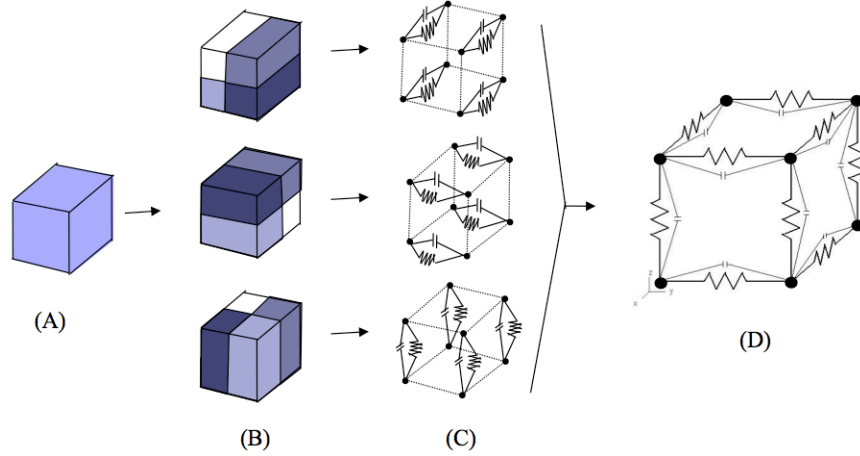


Figure 3.7: Network generation. Each single voxel (A) is considered as a linear composition of three orthogonal components (B), and each edge impedance (C) models one quarter of the voxel in a given direction. The complete model (D) is obtained by superposition.

$$R_x = \frac{1}{\sigma_x} \frac{\Delta x}{\Delta y \Delta z} \quad (3.7)$$

$$C_x = \epsilon_x \frac{\Delta y \Delta z}{\Delta x} \quad (3.8)$$

### Network Generation Algorithm

Generating the equivalent lumped-element circuit can then be accomplished by iterating through each voxel of the model and calculating the equivalent  $R$  and  $C$  for each of its 12 edge impedances using (3.7) and (3.8). The equivalent circuit for the whole voxel is built by connecting all the lumped circuitual elements to the respective nodes, as shown in Figure 3.7. Similarly, the equivalent network for the complete model is obtained by considering all the voxels.

For the proposed solution methods, power is introduced in the model by current injection into the appropriate nodes. Excitation signals other than current sources are transformed into current sources. For instance, voltage sources can be accounted for by adding a series source resistor and obtaining the Norton equivalent to produce an

admittance in parallel to a current source. Similarly, if power is introduced into the model by means of a varying magnetic field, this is reduced to an electromotive force using Faraday's Law, which in time is transformed to a current injection into the appropriate nodes.

### 3.1.4 System Solution

Once the equivalent network is obtained, a linear system can be formed and solved for the node voltages. Depending on the model and the excitation, three different formulations are presented in the following sections, appropriate for static, frequency domain, and time domain solutions of the problem.

### 3.1.5 Static Solution

The static solution constitutes the simplest case, in which all current sources are DC, and all equivalent capacitances in the circuit are completely charged. Under these conditions, capacitors are replaced by open circuits, and the network can be considered purely resistive. Nodal analysis is used to create a suitable linear system, considering  $m$  nodes, and excluding ground. The system is solved for the voltage value at each node.

$$G V = I \quad (3.9)$$

The resulting linear system is of the form (3.9), where  $G$  is the sparse symmetric admittance matrix representing the model's admittance,  $V$  is the unknown voltage vector, and  $I$  the vector describing the currents being injected at each node.

#### Forming the Admittance Matrix $G$

If the network has  $m + 1$  nodes,  $G$  is the  $m \times m$  conductance matrix; each node of the network is present in both the rows and the columns of the matrix. The ground node is implicit.  $G$  is formed from the network resistors by using the following steps derived from nodal analysis:

1. Nodes are sequentially labeled from 1 to  $m$ . Ground node is not counted.
2. All values of  $G$  are initialized to zero.

3. For each pair of nodes  $(a,b)$ :

(a) If  $a = b$ , and there are  $K$  resistances connected to the node:

$$G_{a,b} = \sum_{k=1}^K \frac{1}{R_k}$$

(b) If  $a \neq b$ , and the nodes have  $K$  resistances connected between them:

$$G_{a,b} = G_{b,a} = - \sum_{k=1}^K \frac{1}{R_k}$$

The resulting system will yield a sparse symmetric  $G$  matrix.

### Forming the Current Vector $I$

The  $I$  current vector describes the independent current sources connected to the network. These are the vehicle to inject energy into the model. There is one entry for each node in the system, labeled from 1 to  $m$ .

1. Nodes are sequentially labeled from 1 to  $m$ , using the same order used in  $G$ . Ground node is not counted.
2. All values of  $I$  are initialized to zero.
3. For each current source  $i$  having its positive terminal connected to node  $a$  and its negative terminal connected to node  $b$ :

(a) If  $a$  is the ground node:

$$I_b = I_b - i$$

(b) If  $b$  is the ground node:

$$I_a = I_a + i$$

(c) If neither  $a$  or  $b$  are the ground node:

$$I_a = I_a + i$$

$$I_b = I_b - i$$

## Solving the Linear System

In order to minimize computer memory usage, it is desirable to keep the admittance matrix sparse while solving the linear system; this makes direct methods such a Gaussian elimination a poor choice for this problem. Some authors report using successive overrelaxation (SOR) [34, 35, 39]. In our experience, Krylov sub-space iterative gradient-descent methods have proved effective. The results presented in Chapter 4 and Chapter 5 use the bi-conjugate gradient method implementation from the IML++ library [47].

### 3.1.6 Frequency Domain Solution

Solving the system in frequency domain should be considered when the excitation waveform is sinusoidal or when the applied waveform is such that it can be reasonably approximated by a small number of terms of a Fourier decomposition. In this case, the system to solve will still have the form of (3.9), but  $G$ ,  $V$ , and  $I$  will hold complex values to account for magnitude and phase information. The admittance matrix  $\mathbf{G}$  will be formed using complex impedances instead of resistances as in the static solution.

$\mathbf{G}$  can be formed from the values of the capacitors and resistors connected between two nodes  $a$  and  $b$ , and the angular frequency  $\omega$  using the following steps:

1. Nodes are sequentially labeled from 1 to  $m$ . Ground node is not counted.
2. All values of  $\mathbf{G}$  are initialized to  $(0 + j0)$ .
3. For each pair of nodes  $(a,b)$ :
  - (a) If  $a = b$ ,

- i. If there are  $K$  resistances connected to the node:

$$\Re(\mathbf{G}_{a,b}) = \sum_{k=1}^K \frac{1}{R_k}$$

- ii. If there are  $K$  capacitances connected to the node:

$$\Im(\mathbf{G}_{a,b}) = j\omega \sum_{k=1}^K C_k$$

- (b) If  $a \neq b$ ,

i. If there are  $K$  resistances connected between them:

$$\Re(\mathbf{G}_{a,b}) = \Re(\mathbf{G}_{b,a}) = - \sum_{k=1}^K \frac{1}{R_k}$$

ii. If there are  $K$  capacitances connected between them:

$$\Im(\mathbf{G}_{a,b}) = \Im(\mathbf{G}_{b,a}) = -j\omega \sum_{k=1}^K C_k$$

Accordingly, the current vector  $\mathbf{I}$  will contain the magnitude and phases of the excitation currents for each node. In all other aspects, the process is analogous to the solution of the static case. The solution vector  $\mathbf{V}$  provides the magnitude and phase of voltage at the given frequency for every node in the model.

### 3.1.7 Time Stepping Solution

Time-stepping is computationally more expensive than static or frequency domain cases as it involves solving the linear system once per time step; however, it does provide a solution for transient response using arbitrary waveforms for excitation. In the equivalent network, capacitors are used as energy storage components. To solve the system we first consider initial conditions as defined by our static case, and time-step the system at regular intervals, including the effect caused by the charging or discharging of the network capacitances in terms of current injected or extracted from each network node. This approach is not unlike what has been described by Nagel in [48] and posterior works.

It is of interest to express the current-voltage relation in a capacitor using a numerical treatment that is compatible with both time-stepping and the expression of the linear system (3.9). A possible formulation will now be derived; starting from the differential formulation of the current-voltage relation in a capacitor (3.10), it can be observed that it has the form of an initial value problem (3.11).

$$i(t) = C \frac{dv}{dt} \tag{3.10}$$

$$y'(t) = f(t, y(t)) \quad , \quad y(t_0) = y_0 \tag{3.11}$$



Working with 3.11, and approximating the derivative as a first order finite difference and considering a small interval  $h$  of the function's domain,

$$y'(t) = \frac{y(t) - y(t - h)}{h} \quad (3.12)$$

Rearranging,

$$y(t) = y(t - h) + h y'(t) \quad (3.13)$$

From (3.11) and (3.13), and considering discrete numerical intervals, we arrive at the Backward Euler formula,

$$y_{n+1} = y_n + h f(t_{n+1}, y_{n+1}) \quad (3.14)$$

From (3.10) and (3.11) we can write

$$f(t, y(t)) = \frac{dv}{dt} = \frac{i(t)}{C} \quad (3.15)$$

which can be written as (3.16) when considering a discrete time domain and expressing it for the next time-step, assuming that the capacitance does not vary over time.

$$f(n + 1, y_{n+1}) = \frac{\Delta v_{n+1}}{\Delta t_{n+1}} = \frac{I_{n+1}}{C} \quad (3.16)$$

Finally, from (3.14) and (3.16), the discrete-time linear approximation to the voltage at the terminals of the capacitor over time is given by (3.17).

$$v_{n+1} = v_n + \frac{h}{C} I_{n+1} \quad (3.17)$$

The equivalent circuit for (3.17) is shown in Figure 3.8. Note that  $\frac{h}{C}$  has dimensions of a resistance. Since this circuit configuration introduces an extra node equation per capacitor and uses a voltage source, it is more compact and convenient to represent it by using a Norton equivalent.

$$I_{eq} = \frac{C}{h} V_n \quad (3.18)$$

The final equivalent model for the capacitance is shown in Figure 3.9. From Figure 3.9, it can be observed that a capacitor can be modeled by considering a resistance between

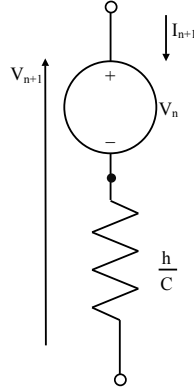


Figure 3.8: Capacitor series linear equivalent.

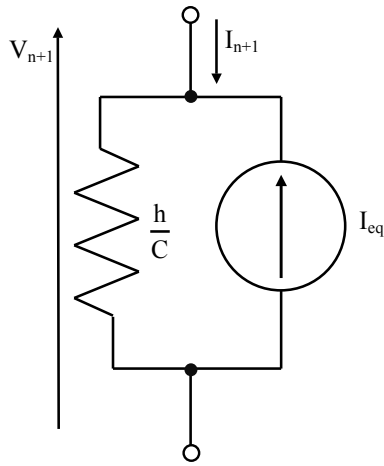


Figure 3.9: Capacitor parallel linear equivalent model. Equivalent current  $I_{eq}$  is calculated using (3.18)

the nodes in parallel with a current source  $I_{eq}$ . The current  $I_{eq}$  injected at each time step will vary depending on the voltage  $V_n$  between the nodes at the last iteration according to (3.18). This current is considered constant for the duration of each time step. A new current vector  $N$  is used to introduce the varying  $I_{eq}$  current for each node at each time step. If multiple capacitors are connected to a node, the corresponding currents are added accordingly. The resulting system has the form described in (3.19)); in it,  $N$  is updated and the system solved for  $V$  at each time step.

$$G_{eq}V = I + N \quad (3.19)$$

The modified matrix  $G_{eq}$  is the admittance matrix, calculated as described in the Static Solution section, but considering the parallel admittances  $\frac{C}{h}$  for each capacitance in the network. As before,  $V$  is the unknown voltage vector,  $I$  the independent current sources vector, and  $N$  the vector describing the displacement current contributed by the charging and discharging of the capacitors during the most recent time step. The initial conditions for the system are determined under DC conditions, that is, all capacitors are considered open circuits and all values of  $N$  set to zero for the first iteration.

After an appropriate value for the time step increment  $s$  is chosen, simulating a period of duration  $d$  involves solving  $n = \lceil \frac{d}{s} \rceil$  time steps. Solving the system involves the sequence of steps described below.

### Time-stepping Algorithm

#### 1. Determining initial conditions:

- (a) Initialize the admittance matrix  $G_{eq}$  from the equivalent impedance network, considering all capacitors as open circuits. This is equivalent to considering only the real part of the impedance, as described when populating  $G$  for the static solution case.
- (b) Initialize the voltage vector  $V$  to best-guess values. If no best-guess values are available, all elements of  $V$  are initialized to 0.
- (c) Initialize the current vector  $I$  to the instantaneous values for all current sources at  $t = 0$ . This is equivalent to how  $I$  was populated in the static case.
- (d) Solve the system  $G_{eq}V = I$  for  $V$ .
- (e) Save the voltage vector  $V$  as the solution of the system for time  $t = 0$ .

#### 2. Initializing for time-stepping:

- (a) Initialize the admittance matrix  $G_{eq}$  from the equivalent impedance network, this time considering the admittances  $\frac{C}{h}$  for each capacitance in addition to the resistors.
- (b) Initialize all elements of the current vector  $N$  to zero.
- (c) Initialize  $s$ , the time-step interval, to the duration of each time interval.
- (d) Set the variable  $n$ , indicating the current time-step, to 0.

### 3. Time-stepping

- (a)  $n = n + 1$
- (b) Fill the current vector  $I$  using the instantaneous value for each current source for  $t = n \times s$ . The procedure is analogous to how  $I$  was populated in the static case.
- (c) Set the value for each element of  $N$  using (3.18). Procedure is similar to how  $I$  was populated in the static case, but considering each capacitor's equivalent current source instead of independent current sources.
- (d) Solve the system  $G_{eq}V = (I + N)$  for  $V$ .
- (e) Save  $V$  as the solution of the system for time  $t = n \times s$
- (f) If  $n < total\ number\ of\ iterations$ , repeat from step 3.

The same numerical techniques used to solve the static solution case are used to solve the linear systems at steps 1.e and 3.d.

## 3.2 Post-processing

Post-processing has proven to be valuable in reducing local artifacts in the calculated scalar potential field caused by discretization.

### 3.2.1 Voltage Interpolation

The result of the admittance method computation is the value of the voltages at every node. In our multiresolution scheme, network nodes are located at the vertexes of voxels. Because conductivity value is considered constant inside each voxel, trilinear interpolation is used to calculate the voltage at arbitrary points inside a voxel from the values at the voxel's vertexes.

Trilinear interpolation has proved useful to generate a fixed spacing discrete electric potential map from a multiresolution result set. This provides a more accurate result than considering the the same value of voltage for all the points inside a voxel, as the truncation error resulting from discretization is reduced. Further, when close to material boundaries, or when plots for different magnitudes such as current density, voltage, and

electric field must be correlated, it is often better to refer all values to the center of a voxel instead of to a corner; trilinear interpolation was used again to refer voltage values to the center of the unit voxel.

### 3.2.2 Calculation of Current Density $\vec{J}$

Current density  $\vec{J}$  for each voxel can be calculated from the conductivity  $\sigma$  and the electric field  $\vec{E}$  using (3.20).

$$\vec{J} = \sigma \vec{E} \quad (3.20)$$

When working with a static simulation, in the most general case  $\sigma$  can be expressed as a rank two tensor as shown in (3.21).

$$\sigma = \begin{bmatrix} \sigma_x & 0 & 0 \\ 0 & \sigma_y & 0 \\ 0 & 0 & \sigma_z \end{bmatrix} \quad (3.21)$$

Similarly, if the system is being solved in the frequency domain, the expression for  $\sigma$  will be (3.22).

$$\sigma = \begin{bmatrix} \sigma_x + j\omega\epsilon_x & 0 & 0 \\ 0 & \sigma_y + j\omega\epsilon_y & 0 \\ 0 & 0 & \sigma_z + j\omega\epsilon_z \end{bmatrix} \quad (3.22)$$

Finally, if the system is being solved for time stepping,  $\sigma$  must consider the admittance added by the capacitors using the linear approximation, and in the general case of an anisotropic material, from (3.8), its expression is given by (3.23).

$$\sigma = \begin{bmatrix} \sigma_x + \left(\frac{h}{4\epsilon_x\Delta x}\right) & 0 & 0 \\ 0 & \sigma_y + \left(\frac{h}{4\epsilon_y\Delta y}\right) & 0 \\ 0 & 0 & \sigma_z + \left(\frac{h}{4\epsilon_z\Delta z}\right) \end{bmatrix} \quad (3.23)$$

### 3.2.3 Calculation of Electric Field $\vec{E}$

Once the voltages have been interpolated back to unit resolution, the  $\vec{E}$  field can be calculated at any instant  $t$  and at any point  $(i, j, k)$  in the model from the instantaneous

voltages at  $t$  and using (3.24). The value  $\Delta s$  is the size of a unit voxel.

$$\vec{E} = \frac{V_{i+1,j,k} - V_{i,j,k}}{\Delta s} \hat{x} + \frac{V_{i,j+1,k} - V_{i,j,k}}{\Delta s} \hat{y} + \frac{V_{i,j,k+1} - V_{i,j,k}}{\Delta s} \hat{z} \quad (3.24)$$

The value calculated by (3.24) is referred to a corner of a voxel. To have the  $\vec{E}$  value referred to the center of each voxel (3.31), the interpolated voltages at the center of each face of the voxel are considered instead of the voltages at the vertices. Center face voltages for the voxel having its lower, left, back corner at  $(i, j, k)$  can be calculated using the expressions below.

$$\bar{V}_{up} = \frac{V_{i,j,k+1} + V_{i+1,j,k+1} + V_{i+1,j+1,k+1} + V_{i,j+1,k+1}}{4} \quad (3.25)$$

$$\bar{V}_{dn} = \frac{V_{i,j,k} + V_{i+1,j,k} + V_{i+1,j+1,k} + V_{i,j+1,k}}{4} \quad (3.26)$$

$$\bar{V}_{lt} = \frac{V_{i,j,k} + V_{i+1,j,k} + V_{i+1,j,k+1} + V_{i,j,k+1}}{4} \quad (3.27)$$

$$\bar{V}_{rt} = \frac{V_{i,j+1,k} + V_{i+1,j+1,k} + V_{i+1,j+1,k+1} + V_{i,j+1,k+1}}{4} \quad (3.28)$$

$$\bar{V}_{ft} = \frac{V_{i+1,j,k} + V_{i+1,j+1,k} + V_{i+1,j+1,k+1} + V_{i+1,j,k+1}}{4} \quad (3.29)$$

$$\bar{V}_{bk} = \frac{V_{i,j,k} + V_{i,j+1,k} + V_{i,j+1,k+1} + V_{i,j,k+1}}{4} \quad (3.30)$$

$\bar{V}_{up}$ ,  $\bar{V}_{dn}$ ,  $\bar{V}_{lt}$ ,  $\bar{V}_{rt}$ ,  $\bar{V}_{ft}$ , and  $\bar{V}_{bk}$  refer to the voxel's voltages at the center points of its up, down, left, right, front and back faces, as illustrated in Figure 3.10. The center face voltage values are calculated using (3.31).

$$\vec{E}_{center} = \frac{\bar{V}_{ft} - \bar{V}_{bk}}{\Delta s} \hat{x} + \frac{\bar{V}_{rt} - \bar{V}_{lt}}{\Delta s} \hat{y} + \frac{\bar{V}_{up} - \bar{V}_{dn}}{\Delta s} \hat{z} \quad (3.31)$$

### 3.2.4 Calculation Equivalent Resistance

Equivalent resistance as measured between an electrode injecting current and the current return can be readily calculated by injecting a continuous current of 1 A in the stimulating electrode, and solving the model for static conditions. Then, the voltage value reported at the tip of the current-injecting electrode will be numerically equivalent to the resistance between electrodes.

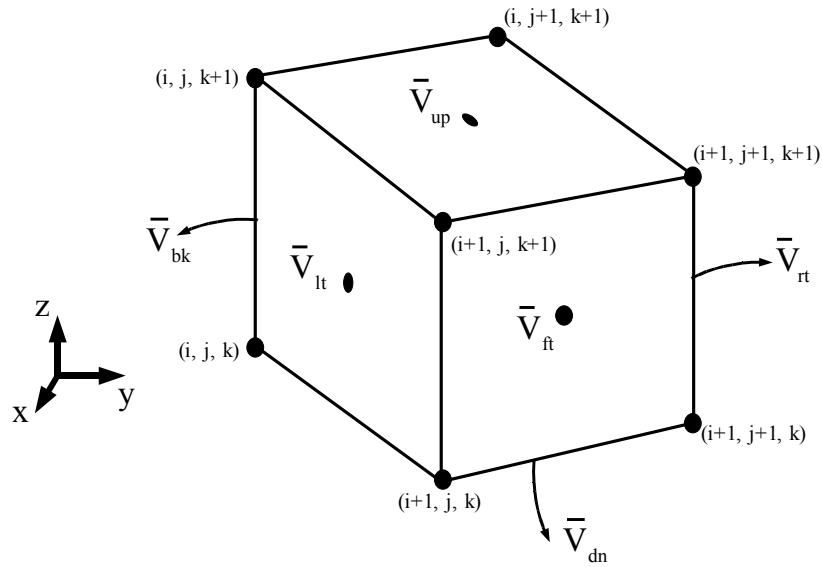


Figure 3.10: Position for center-face voltages of a voxel.  $\bar{V}_{bk}$ ,  $\bar{V}_{rt}$ , and  $\bar{V}_{dn}$ , indicated with arrows in the figure, are in the center of the respective non-visible faces of the voxel.

### 3.3 Method Verification and Error

It is of interest to characterize the performance of the method as described. Accurate numerical solution of large, complex numerical models can be challenging, as many factors influence the results. In addition to the quasi-static and frequency dispersion approximations, several sources of errors common to all time-stepping numerical electromagnetic methods exist; they include modeling error, spatial discretization error, time quantization, numerical approximation because of the use of iterative solving methods, and numerical rounding. Moreover, when using iterative solvers, convergence is not guaranteed for all possible cases. While intuitively it may appear that using a small grid will result in a more precise numerical approximation, this is not necessarily the case, as decreasing the voxel size in a model does not guarantee a smaller error in every case. The cause of this is described in Figure 3.12: Since the smooth function describing the behavior of the system is approximated by the values at the network nodes, the *truncation error* will be smaller. However, smaller voxel sizes will result on closer numerical values at neighboring nodes, causing an increase in the round-off error associated with differences of similar numbers, and increasing overall error [49]. The numerical representation used

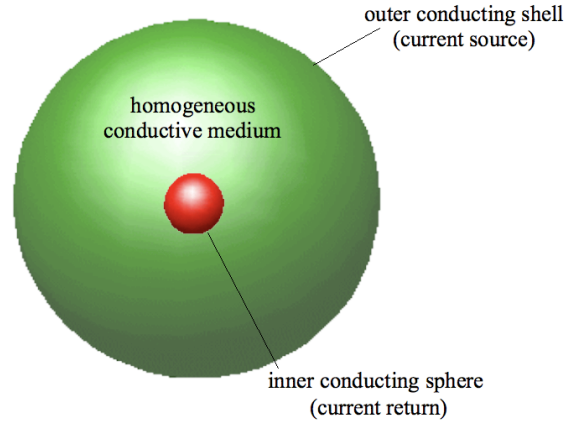


Figure 3.11: Model for method verification.

by the computer system weights heavily on round-off error as well.

In most situations, a reasonable trade off of computational resources versus precision can be achieved. Spatial discretization error is particularly influenced by model geometry and level of detail. Time discretization is sensitive to the high frequency components of excitation waveforms, and numerical rounding can be corrected to some degree by using more precise numerical representations and appropriately scaling the linear system before solving. Convergence can be improved using adequate preconditioning of the admittance matrix, and precision of the solution can be increased by setting a smaller error criteria to stop iterating.

Since the magnitudes of error vary depending on the model's ratio of unit resolution to minimum feature size, excitation source, and implementation of the formulation, the approach taken to characterize error was to consider a model that can be analytically solved and measure relative error in the numerical solution versus the analytical one. A model and two test cases were devised to verify the proposed impedance method formulation. The first case considers the static solution for every point in the model, and the second case a solution at one point over time. The geometry of the model used for both cases is identical, and pictured in Figure 3.11, and consists of a solid metallic sphere of radius  $r_1 = 5 \text{ cm}$  surrounded by a concentric spherical metallic shell of radius  $r_2 = 50 \text{ cm}$ . A current source is connected between the shell and the inner sphere, which acts as a current return. The interstitial material between the inner sphere and the shell was different for each simulation, as described in the respective sections below.



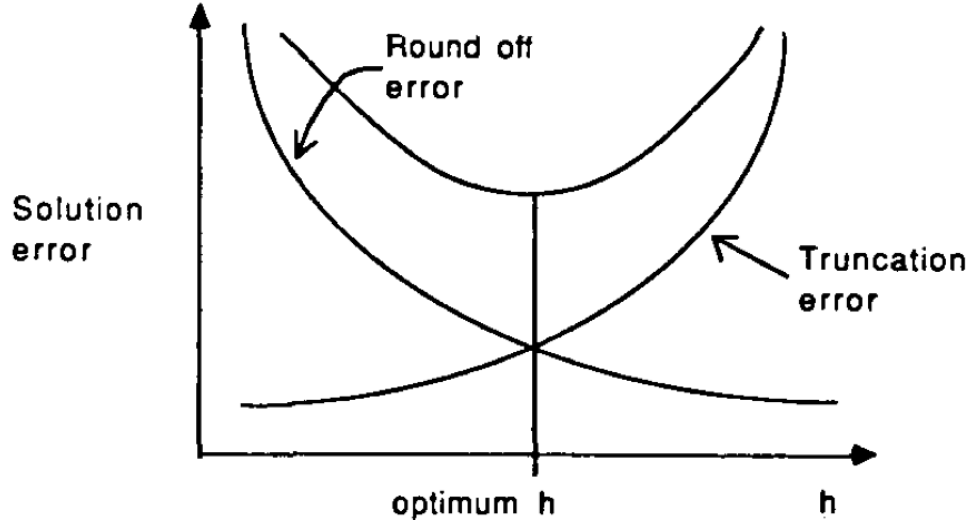


Figure 3.12: Overall solution error as a combination of round-off error and truncation error.  $h$  denotes the voxel size used in the model. Because of computer memory constraints, in general, simulations tend to operate towards the right of the optimum size. Plot reproduced from [49].

The entire assembly was positioned in a slightly larger cubic space, measuring 1 m per side. The model was partitioned into cubic voxels having 0.5 cm sides, for a total size of  $220 \times 220 \times 220$  unit voxels.

$$e_{rel} = \left( 1 - \frac{V_{IM}}{V_{analytical}} \right) \times 100 \quad (3.32)$$

Not all points in the model will have the same error. The largest errors tend to occur immediately next to the current injection points; this is expected, because the current densities will be larger close to the source, and for the same material conductivity, the  $\vec{E}$  field will be larger, and since the space is partitioned in voxels, the relative errors for voltage will be larger for the same voxel size than at distant parts of the model. This effect can be minimized by setting the current injection points inside large homogeneous volumes and using guide points to ensure an even spread of current from the injection point.

## Overall Relative Error Calculation

Because the direct result of the impedance method is the scalar potential field over the volume of the model, it is of interest to determine the error for voltages. Relative percentage error for one point  $e_{rel}$  was defined as per (3.32), where  $V_{IM}$  is the voltage resulting from the Impedance Method simulation at the node corresponding to the point in question, and  $V_{analytical}$  is the voltage for the same point obtained using an analytical solution for the same problem. The overall relative error for a simulation was computed by sorting all the simulation points by their relative error, considering the 99% of points having the lowest error, and reporting the maximum relative error for that group.

### 3.3.1 Static Case

The three dimensional model shown in Figure 3.11 represents the spherical capacitor used as a test case for the method. The interstitial material between the inner sphere and the outer shell was considered to be purely resistive, having a conductivity of  $\sigma = 1 \text{ s} \cdot \text{m}^{-1}$ . The center sphere and the outer spherical shell were modeled as metals, with a conductivity of  $\sigma_{metal} = 1e10 \text{ s} \cdot \text{m}^{-1}$ . The space outside the outer shell was filled with metal for our simulation.

The voltage at any point in the interstitial medium was calculated as a function of the distance from the center of the inner sphere by integrating successive spherical resistive layers having a differential thickness using (3.33). Multiple cases were considered. A simulation of the uniform resolution at  $0.5 \text{ cm}$  was executed in addition of the multi-resolution cases to evaluate the multiresolution algorithm. Cases with and without guide points were considered as well. For all simulations in this series using guide points, the parameters used were  $a = 0.12$  and  $b = 0$  (3.2).

$$V(r) = \frac{I}{4\pi\sigma} \int_{r_1}^r \frac{1}{r^2} dr = \frac{I}{4\pi\sigma} \left( \frac{1}{r_1} - \frac{1}{r} \right) \quad (3.33)$$

A summary of the results is presented in table 3.1, and corresponding plots in Figure 3.18. In Table 3.1, the *Clustering Strategy* column describes the type of model, uniformly sized or a multiresolution, and if guide points at the current return and current injection points were used or not. The *Maximum Voxel Size* column specifies the maximum size allowed for clustering in the multiresolution algorithm relative to unit voxel

Table 3.1: Static Solution Results.

Clustering Strategy	Maximum Voxel Size	Number of Voxels	Relative Model Size (%)	Overall Relative Error (%)
Uniform resolution	1	10648000	100.0	5
Multi-resolution	2	1703752	16.0	8
Multi-resolution	4	662507	6.2	21
Multi-resolution	8	553141	5.2	39
Multi-resolution	16	545144	5.1	97
Multi-resolution + GP	2	1729589	16.2	5
Multi-resolution + GP	4	698094	6.6	8
Multi-resolution + GP	8	593615	5.6	8
Multi-resolution + GP	16	588574	5.5	7

size. The *Relative Model Size* indicates the size of the model relative to the uniform resolution case. Relative error distribution was observed to be sharper for cases where guide points were not used. This was expected, as guide points allows for a smooth spread of currents across a large number of nodes, which tends to minimize error dispersion for homogeneous volumes. Figures 3.13 and 3.14, shows the relative error distribution for the two multiresolution cases having a maximum voxel size of four, one using guide points at the sources and the other not. Figures 3.15 and 3.16 show the results for maximum voxel size of 16. It can be observed that the relative error is significantly smaller when using guide points in both cases.

Another dimension that was explored for this model was the Bi-conjugate Gradient method numerical convergence behavior for the linear system. The intention was to determine what value for normalized residue was appropriate to use as a stop criteria for similar models. Additionally, it was of interest to determine if the system would gradually converge to a solution or if the convergence would be fast, and once reached, if further error reduction could be achieved by executing extra iterations. For this, a simulation set was created and multiple runs were executed, restricting the normalized residue value used as criteria to stop iterating to an increasing number for each run. Results from this set are shown in figure 3.17, and they suggest that once a reasonably low criteria is reached, error does not further reduce with extra iterations. From the plot, it can be observed that the normalized residue value for convergence in this model is in the order

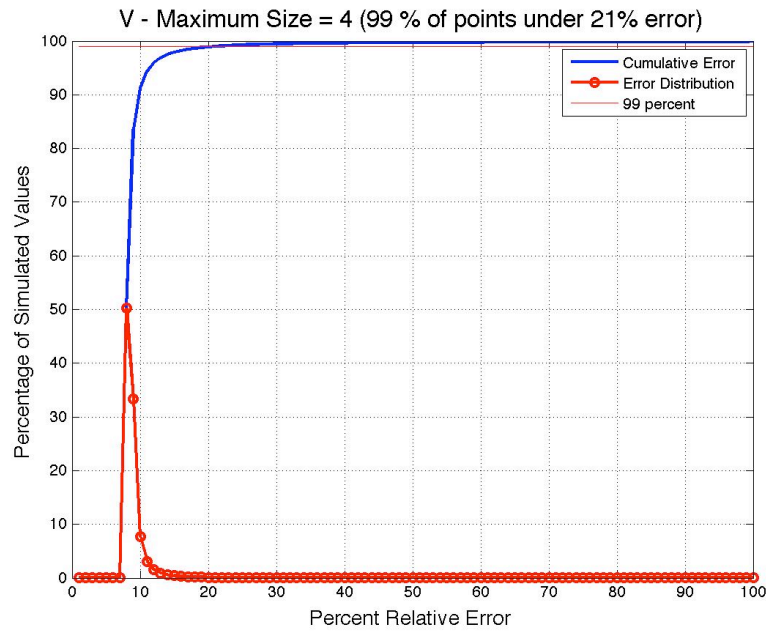


Figure 3.13: Impedance Method error distribution for the Static Case model and multi-resolution clustering having a maximum size of 4.

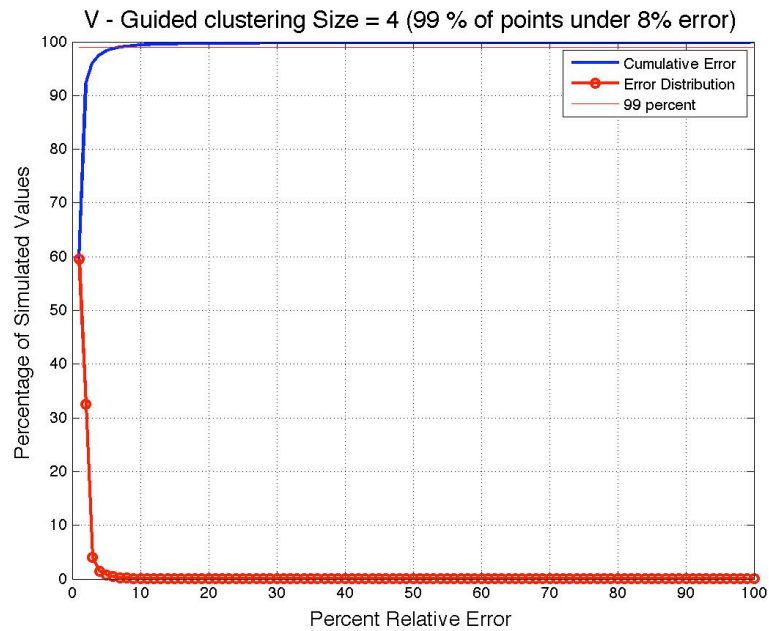


Figure 3.14: Same case as Figure 3.13, but using guide points.

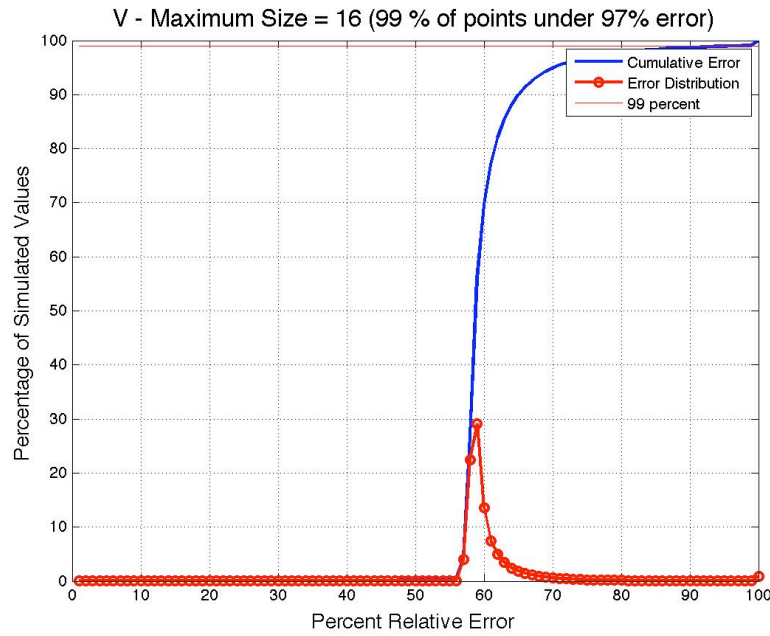


Figure 3.15: Impedance Method error distribution for the Static Case model and multi-resolution clustering having a maximum size of 16.

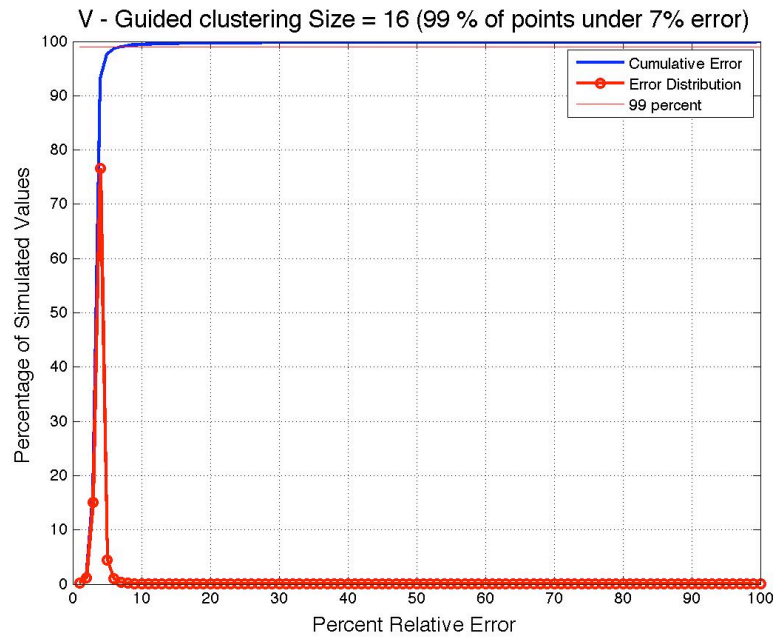


Figure 3.16: Same case as Figure 3.15, but using guide points.

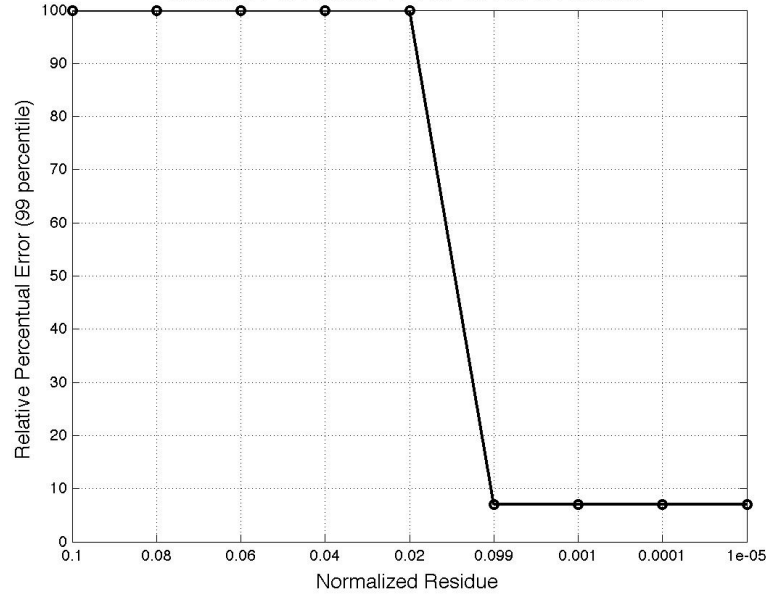


Figure 3.17: Relative error as a function of the residue stop criteria. All the data points correspond to the static case, using multiresolution clustering with guide points at both the current injection and current return points. The maximum normalized voxel size used for clustering on this simulation set was 16.

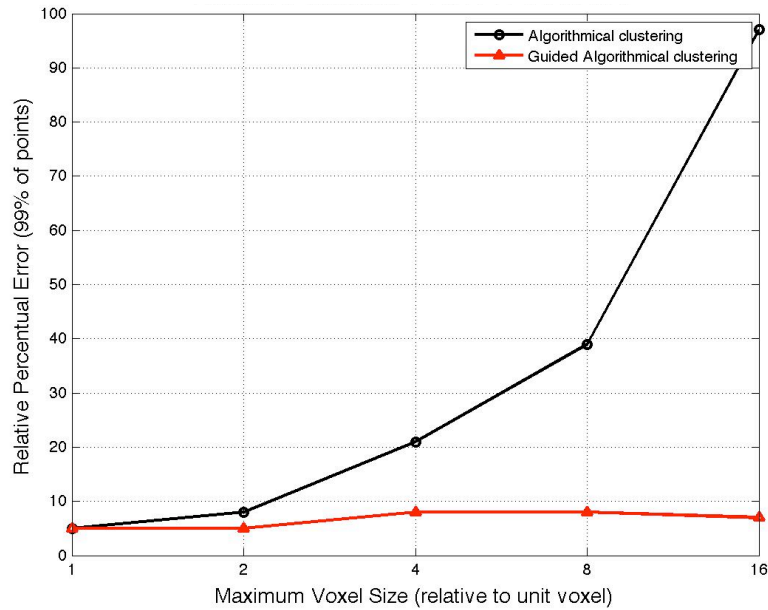


Figure 3.18: Relative error as a function of the maximum voxel size allowed for clustering. Using guide points at the source and return allows to keep the relative error low independently of the maximum voxel size, permitting simulation of larger models with the errors closer to the uniform resolution case.

of  $10^{-2}$ ; from this, the value adopted as normalized residue criteria to stop iterating in all simulations in Chapter 4 was  $10^{-7}$ , five orders of magnitude smaller.

### 3.3.2 Time Varying Case

The time varying case was used to verify the time domain algorithm. For this case, the setup described in Figure 3.11 was used to model charging a spherical lossy capacitor. The multiresolution clustering algorithm was applied, allowing a maximum cluster size of 16 unit voxels. Two guide points were used, one at the current source and one at the current return. Initial conditions considered the capacitor was discharged. A 1A current step starting at  $t = 0$  was injected in the outer shell, while the inner sphere was set to ground.

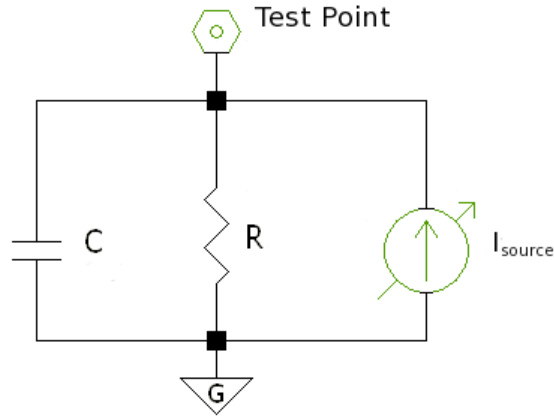


Figure 3.19: Canonical network model for spherical lossy capacitor.

For purposes of comparison, results for a canonical equivalent model shown in Figure 3.19 were obtained. The errors reported in this section were obtained by contrasting the voltage obtained by the numerical solution of the model at the current injection point using the time-stepping impedance method with the canonical solution for the voltage at the test point in the circuit shown in Figure 3.19 and given by (3.34).

$$V_{tp}(t) = V_{TH} \left( 1 - e^{-\frac{t}{RC}} \right) \quad (3.34)$$

The relative error criteria is described by (3.32). As before, the overall error is con-

sidered as the largest error that fits 99% of all the data points considered. While in the previous section the values considered for calculating the relative error represented voltage values for all the points in the model, in the time-stepping case the values considered represent voltages for a given point in the model with respect to ground for each one of the time steps simulated. In (3.34),  $V_{tp}(t)$  is the instantaneous voltage at the test point while charging the capacitor, and  $V_{TH}$  is the Thevenin-equivalent voltage source for  $I_{source}$  at Figure 3.19, which is equal to the numerical value of  $R$ , since  $I_{source} = 1A$ . The relation between the value of  $R$  and the conductivity of the material between the inner sphere and the spherical shell of the impedance method model is shown in (3.35) and can be calculated from Ohm's Law and (3.33).

$$R = \frac{\frac{1}{r_1} - \frac{1}{r_2}}{4\pi\sigma} \quad (3.35)$$

Similarly, the relation between the value of the lossless capacitor  $C$  and the permittivity for the filling material can be determined to be (3.36) from the charge-voltage relation for a capacitor and Gauss's Law for a charged sphere.

$$C = \frac{4\pi\epsilon_0\epsilon_r}{\frac{1}{r_1} - \frac{1}{r_2}} \quad (3.36)$$

To determine the model parameters, an arbitrary relative permittivity of  $\epsilon_r = 10^6$  was chosen. Then, in order to obtain a time constant in the order of few milliseconds, a conductivity  $\sigma = 1.4323 \text{ mS}$  was adopted. The corresponding values for the lumped components for the idealized model were determined to be  $R = 1023.1\Omega$  and  $C = 6.1814 \mu F$  using (3.35) and (3.36). The resulting time constant for the circuit was then  $R \times C \approx 6.32 \text{ ms}$ . The time step chosen was  $s = 0.1 \text{ ms}$  and the total duration of the simulation was 600 steps, close to ten times the time constant, to allow the voltage across the capacitor to converge to a stable value.

Figure 3.20 show the simulation results, contrasted with the analytical solution. The error distribution is reported in Figure 3.21. Overall, when using proper clustering parameters, the method resulted in acceptable errors for numerical simulations.



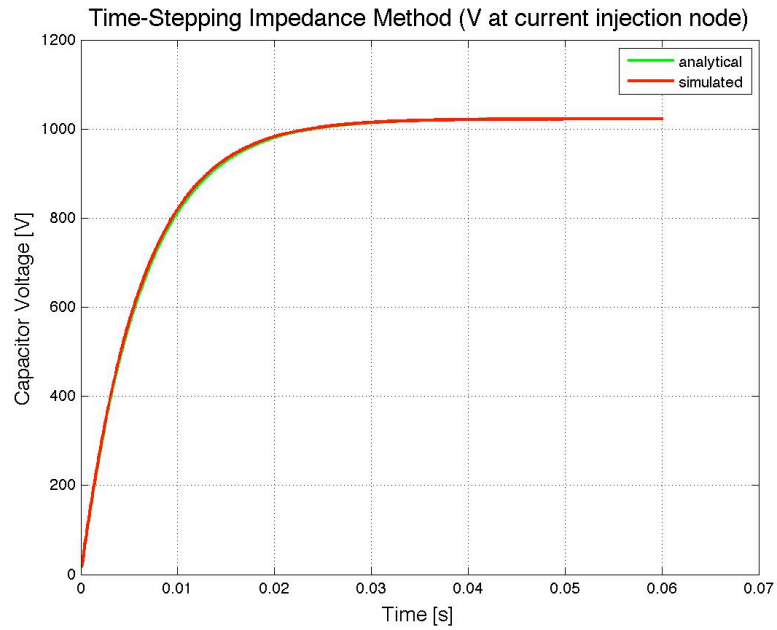


Figure 3.20: Analytical and simulated charging voltages over time for time-stepping test case.

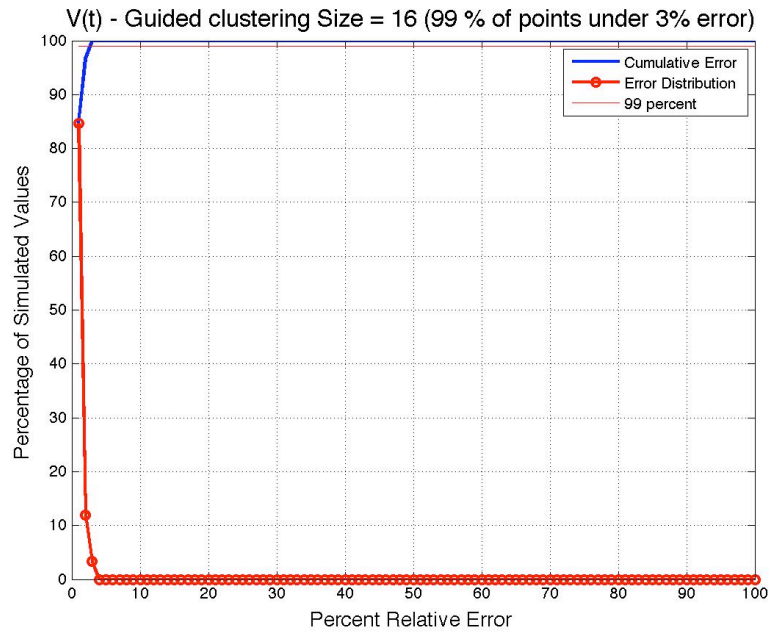


Figure 3.21: Error distribution for the time-stepping simulation.

# Chapter 4

## Applications to Medical Implanted Devices: Retinal Prosthesis

### 4.1 Introduction

For implanted medical devices, the admittance method can provide a way to numerically approximate the current densities, electric potential scalar field, electric and magnetic fields, impedance in between two arbitrary points of the model, dynamics of the interface between metal electrodes and body electrolytes, specific absorption rate (SAR), RMS absorbed power, and more. In general, applications to implanted devices present unique challenges in which it requires model resolutions far greater than the level of detail needed to calculate power absorption by exposure to a varying electromagnetic field, as done in [34] and [35]. This is one of the key reasons why the multiresolution algorithm is important for this type of problem.

The applications of the multiresolution admittance method described in this chapter are in the context of a retinal prosthetic implant to partially restore vision to people suffering from certain degenerative diseases of the eye; however, the principles used are generic and appropriate for modeling of a wide variety of implanted electrical stimulation devices. Retinal degenerative diseases such as Retinis Pigmentosa (RP) and Age Related Macular Degeneration (AMD) progressively disable photoreceptor cells and eventually lead to blindness. In clinical studies, it has been observed that even when photoreceptor cells are no longer active, a large portion of the visual pathway remains relatively healthy in the short term [5]. Furthermore, patients have reported seeing points of light in

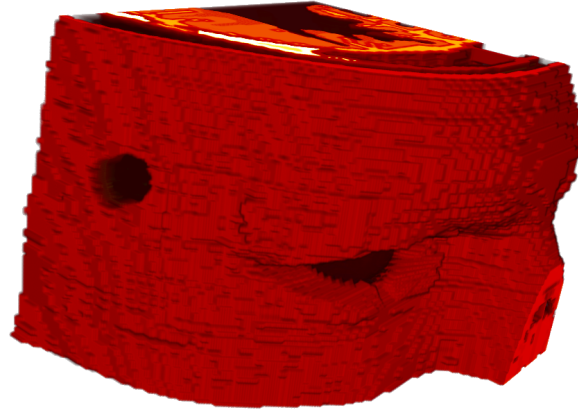


Figure 4.1: Three-dimensional rendering of partial head model used for calculating extraocular (corneal) electric stimulation. Electrodes were positioned in direct contact with the cornea of the eye, and current return was considered in the temporal aspect of the head, shown in the model as a darker cylinder, towards the left side of the figure.

an otherwise blank visual field when probe electrodes were used to inject appropriate amounts of electrical charge in the Ganglion Cell Layer of the retina [7]. Taking advantage that the spatial location of the perceived light appears to correspond to the physical location of the electrical stimulus in the ganglion cell layer (GCL), an implanted retinal electrical stimulator can be used to stimulate the human retina in a systematic way and restore a limited form of vision. The electrical stimulation of the GCL is performed using an implantable electrode array positioned inside the eye, affixed to the retina using a surgical tack. The implantable stimulators allow to partially restore some form of vision to patients blinded by photoreceptor loss; this is achieved by using systematic electrical stimulation of the surviving ganglion and bipolar cells, thus effectively replacing the functionality of the now damaged photoreceptor cells.

It is not clear at this time if retinal implants are a viable long term solution to restore vision, as degenerative diseases tend to progressively remodel retinal neural tissue in complex ways [14, 15]; nonetheless, the studies and simulations presented below address a significant portion of the applications and possibilities of the proposed admittance method to medical implants in general.

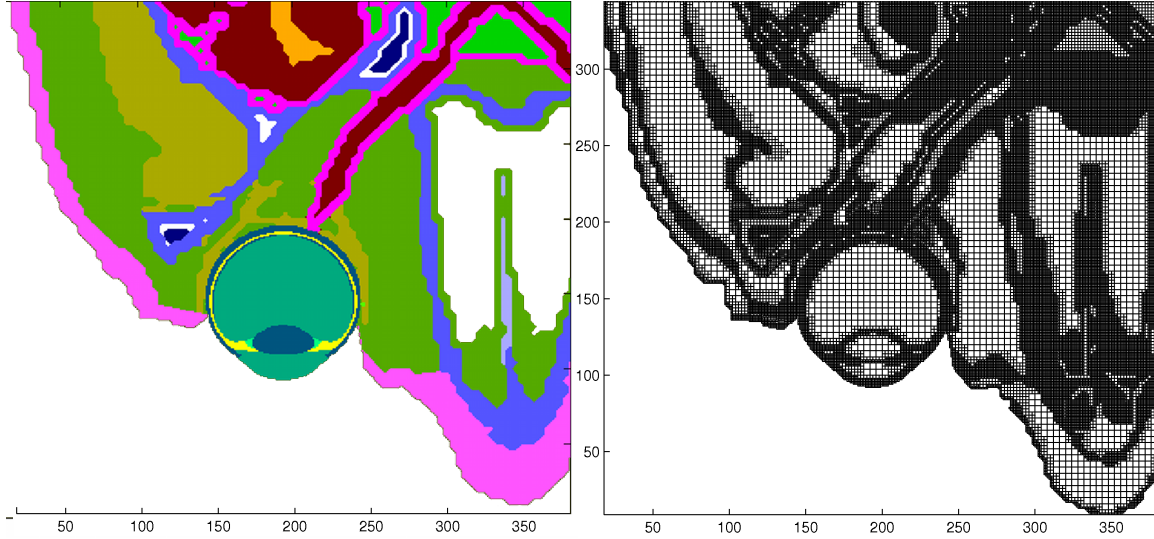


Figure 4.2: Transversal slices of numerical model for extraocular stimulation at the center of the eye (*Left*) and corresponding rendering using the multiresolution algorithm and a maximum voxel size  $M = 4$  (*Right*).

## 4.2 Extraocular Electrical Stimulation

When considering implanting a retinal stimulator, it is desirable to be able to characterize the response of the patient's retina to electrical stimulation prior to surgically implanting a permanent device [5]. The multiresolution admittance method was used to determine the electric potentials at the retinal surface arising from stimulation using corneal electrodes. Two different electrodes, namely a DTL Plus electrode manufactured by Diagnosys LLC, and ERG-Jet manufactured by Fabrinal SA, have been considered as a mean to provide an electrical stimulus on the external surface of the cornea with the intent of exciting visual stimuli (phosphenes), and measuring the ability of the remaining visual path to respond to electrical stimulation.

An anatomically correct partial model of a human head spanning a  $7\text{ cm} \times 8.6\text{ cm} \times 9.5\text{ cm}$  volume, centered around the right eye, and having a resolution of  $250\ \mu\text{m}$  was devised using spatial interpolation from the  $1\text{ mm}$  male dataset of the Visible Human Project [45]. The extents of the model are shown in Figure 4.1, and transverse slices at the center of the eye and at the center of the return electrode shown in Figure 4.2. The size of the model was  $281 \times 345 \times 380$  voxels, and the dielectric properties of the constitutive tissues are listed in Table 4.1. Tissue dielectric properties were collected from

literature [50]. The multiresolution clustering algorithm was applied using a maximum voxel size of  $M = 4$ , which reduced the voxel count by 70%, from 36.8 million voxels to 10.8 million voxels.

Table 4.1: Tissue Conductivities at 100 Hz.

Material	Conductivity ( $\Omega \cdot m$ )
Air	1.00E-020
Blood	7.00E-001
Blood Vessel	2.78E-001
Bone Cancellous	8.10E-002
Bone Cortical	2.01E-002
Bone Marrow	1.82E-003
Brain Grey Matter	8.90E-002
Brain White Matter	5.81E-002
Cartilage	1.72E-001
Cerebro Spinal Fluid	2.00E+000
Eye Cornea	4.22E-001
Eye Lens	3.22E-001
Eye Retina	5.03E-001
Eye Sclera	5.03E-001
Fat	2.08E-002
Glandular Tissue	5.22E-001
Metal	1.00E+010
Mucous Membrane	4.61E-004
Muscle	2.67E-001
Muscle	2.67E-001
Skin (Dry)	2.00E-004
Skin (wet)	4.61E-004
Tendon	3.05E-001
Vitreous Humor	1.50E+000

Two types of corneal electrodes were modeled. The JET electrode is essentially a thin 1 cm diameter ring electrode positioned on the cornea, much like a contact lens, with the current return positioned on the temple. The DTL electrode is a thin conductive wire in contact with the lower frontal aspect of the cornea, where it meets the sclera with,



Figure 4.3: DTL Plus electrode, courtesy of Diagnosys LLC ([www.diagnosysllc.com](http://www.diagnosysllc.com)), by its own (Top Left), and positioned on eye (Top Right). ERG-Jet corneal electrode, courtesy of Fabrinal SA ([www.fabrinal.ch](http://www.fabrinal.ch)), by its own (Bottom Left) and placed on eye (Bottom Right).

again, the current return placed on the temple. Figure 4.3 shows both configurations. Stimulation was provided by a 2 ms, 0.5 mA rectangular current pulse. Fourier analysis was used to determine that the strongest frequency component of the stimulation pulse was close to 100 Hz, so tissue conductivity for that frequency was used.

The system was statically solved using the multiresolution admittance method, obtaining the electrical scalar potential for all points of the problem for the described stimulation signal for each electrode. This resulted in retinal surface voltages ranging from 19.438 V to 19.450 V for the case of the DTL electrodes, and slightly lower values, 19.293 to 19.303 for the Jet electrode.

The voltage values corresponding to the retinal surface were then extracted, and mapped into a rectangular area using a spherical to cylindrical projection of the retinal surface. The resulting retinal surface voltage map is shown in Figure 4.4 and Figure 4.5; the left side of the plots correspond to the optic nerve in the back of the eye, and the

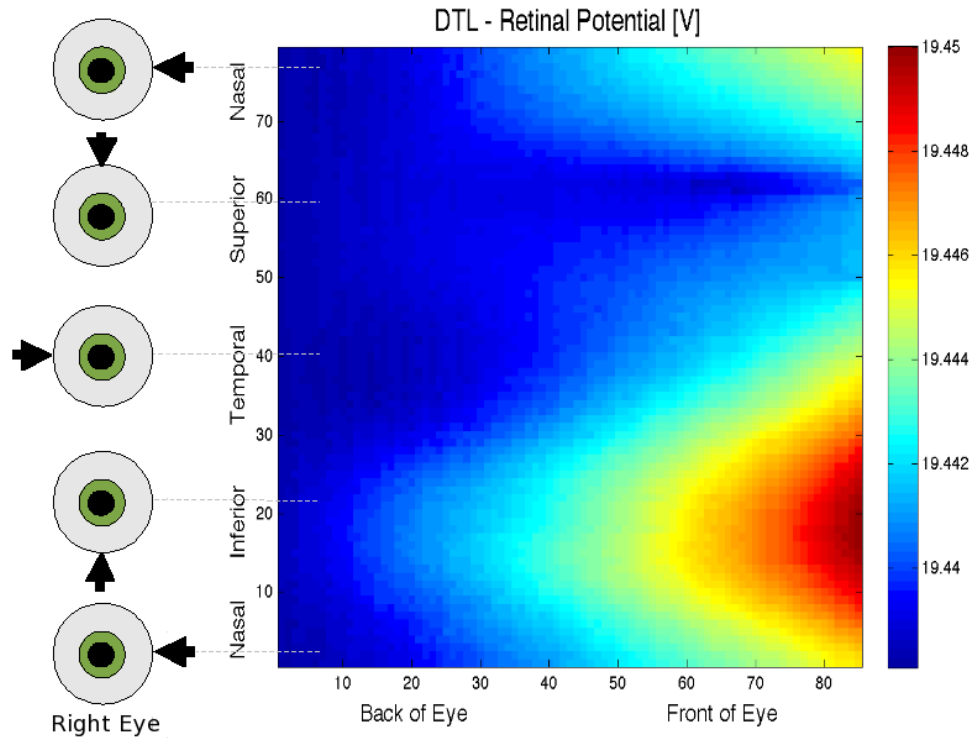


Figure 4.4: Retinal surface voltage map resulting from extraocular stimulation using DTL Plus electrode. The values at the spherical surface of the retina are mapped to a cylindrical surface which is cut at the nasal aspect and unrolled to a rectangular area. Arrows on eye diagrams on the left indicate approximate position of eye for Y axis (looking towards right eye of patient). Left side of plot corresponds to optic nerve, right side corresponds to the frontal portion of the retina.

right side to the frontal edge of the retina. The retinal potential was calculated at the vitreous humor,  $125 \mu m$  from the surface of the retina, using linear interpolation; this location was chosen because the vitreous humor has higher conductivity and a larger homogeneous volume compared to the retina, which helped to obtain a well behaved gradient by interpolation given the constraints in model resolution.

Starting from the retinal surface potentials, the activation function [13] corresponding to the direction of the OFL axons was approximated as the second derivative of the voltage with respect to the direction of the ganglion cell layer axons flowing towards the optic nerve (right to left, horizontal, in the figures) for both Jet and DTL corneal electrodes. Figure 4.6 and Figure 4.7 show the absolute value of the normalized activation function; this should be an appropriate approximation for balanced biphasic pulses in a

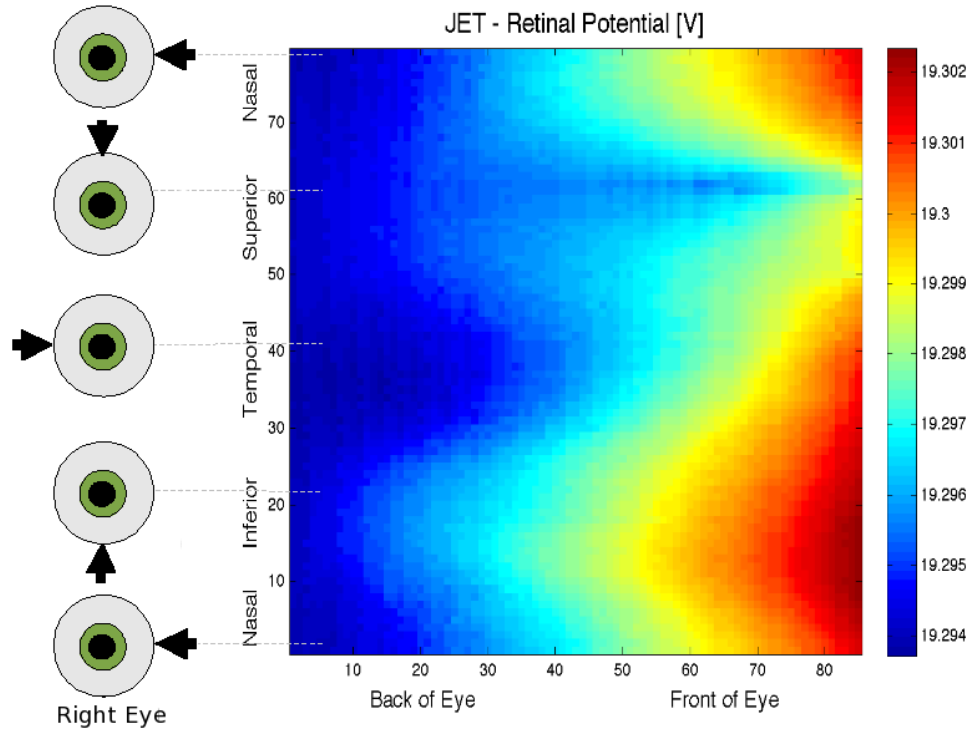


Figure 4.5: Retinal surface voltage map resulting from extraocular stimulation using ERG Jet electrode. The values at the spherical surface of the retina are mapped to a cylindrical surface which is cut at the nasal aspect and unrolled to a rectangular area. Arrows on eye diagrams on the left indicate approximate position of eye for Y axis (looking towards right eye of patient). Left side of plot corresponds to optic nerve, right side corresponds to the frontal portion of the retina.

linear model. In order to generate plots that are directly comparable for both electrode designs, and to account just for the regions where activation is possible, only the positive values were considered in the plots (negative values were considered as zero), and the resulting plot was normalized to a 0 to 1 range. In addition, a  $3 \times 3$  matrix averaging filter was applied to mitigate the effect of the relatively coarse model resolution compared to the thickness of the retina. The vertical striping pattern observed in the activation plots is due to the staircase effect artifacts caused by the simulation meshing process and the resulting voxel size for this set of models. The red circle in Figure 4.7 marks a high local value for the activation function due to an anomaly in the model, and it is present in all simulation runs. At that place in the model the choroid is pinched and the retina is in direct contact with the sclera. This is due to the relatively coarse resolution of the



model.

The resulting activation pattern is strongly concentrated in the retinal surface closer to the electrode in the case of the DTL electrode, while it is evenly distributed for the Jet electrode. Based on this numerical simulation and data from clinical trials, the DTL electrode was considered a better choice for using during the pre-surgical assessment of RP patients. Comparisons of numerical results obtained using this method and available experimental data from patients suffering from RP recorded by Xie *et al* show a remarkable agreement, and have been reported in [41].

### 4.3 Parametric Models for Epiretinal Implantable Electrode Array

In the context of designing better implantable electrode arrays apt for epiretinal electrical stimulation, it was desirable to understand what geometry and constructive parameters influence the performance of the devices. To this effect, a set of simulations were performed, aiming to answer questions including how important is array placement in perfect contact with the retinal surface, how having a near by current return will affect the injected charge distribution, and the effects of electrode size for this particular configuration. The results from each simulation set was tabulated and the resulting curves fitted and expressed as a function of the injected current and other parameters, to gain a qualitative understanding of the impact of individual parameter variation in this configuration.

One of the parameters taken into account for electric stimulator design is the ability of the device to inject and extract electrical charges at the target location. Current density magnitude at the ganglion cell layer (GCL) is a good indicator of the performance of the stimulator, and has been used through this section as an indicator of performance of the implanted device. A model including a flat layered retina and an stimulator consisting in a  $5 \times 5$  electrode array model was constructed. The stimulator array was placed in an epiretinal configuration, with the electrodes embedded in an insulating backing, and the current return at the back of the assembly, as shown in Figure 4.8. The thickness and resistivity of the retinal layers considered was obtained from measurements made on images of microscopic photographs from a mammalian retina [12] and from literature [51], and is described in Table 4.2. For all the simulations, all the electrodes

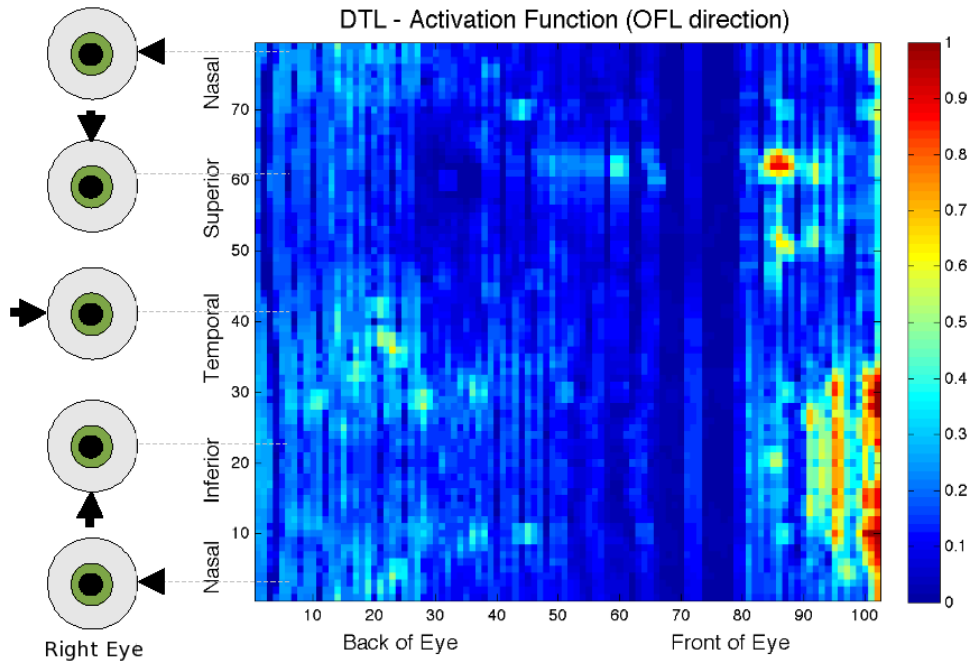


Figure 4.6: Approximation of the activation function resulting from extraocular stimulation using DTL electrode. The values at the spherical surface of the retina are mapped to a cylindrical surface which is cut at the nasal aspect and unrolled to a rectangular area. Arrows on eye diagrams on the left indicate approximate position of eye for Y axis (looking towards right eye of patient). Left side of plot corresponds to optic nerve, right side corresponds to the frontal portion of the retina.

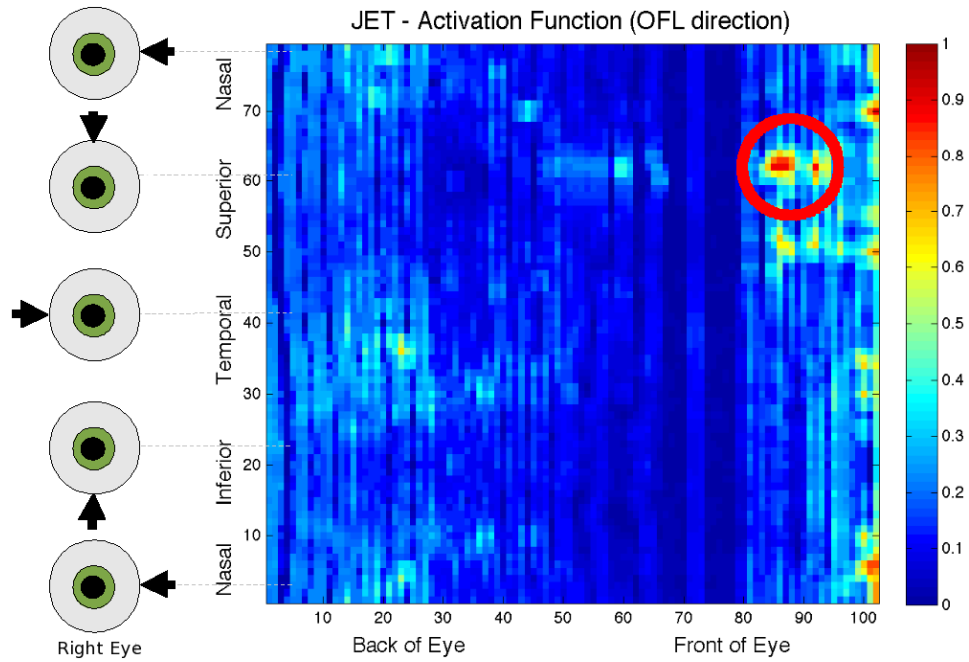


Figure 4.7: Approximation of the activation function resulting from extraocular stimulation using ERG Jet electrode. The values at the spherical surface of the retina are mapped to a cylindrical surface which is cut at the nasal aspect and unrolled to a rectangular area. Arrows on eye diagrams on the left indicate approximate position of eye for Y axis (looking towards right eye of patient). Left side of plot corresponds to optic nerve, right side corresponds to the frontal portion of the retina. The red circle marks anomaly due to pinching of choroid in model, present in both Jet and DTL cases.

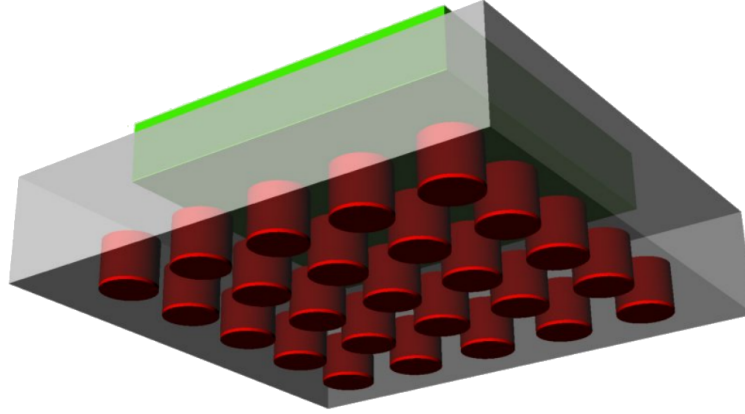


Figure 4.8: Model of  $5 \times 5$  epiretinal electrode array (not to scale).

were considering firing simultaneously, driven by current sources, each injecting  $100 \mu A$ . To resolve the layered structure of the retina, the entire model was discretized at a resolution of  $10 \mu m$ .

Table 4.2: Retinal Layered Model.

Material	Resistivity ( $\Omega \cdot m$ )	Thickness ( $\mu m$ )
Photoreceptors	50.5	62.4
Outer Nuclear Layer (ONL)	60.0	31.2
Outer Plexiform Layer (OPL)	70.0	62.4
Inner Nuclear Layer (INL)	65.0	31.2
Inner Plexiform Layer (IPL)	18.0	31.2
Ganglion Cell Layer (GCL)	70.0	31.2
Nerve Fiber Layer (NFL)	70.0	31.2

### 4.3.1 Effect of Electrode Array Lift-Off

In epiretinal implants, because the implant is positioned by the surgeon through a small opening on the sclera, and the retinal tissue is particularly fragile, the implant cannot always be pressed to perfectly close the gap between the electrode array and the retinal

surface. We will refer to this gap as *lift-off*. Further, in some electrode array designs, the implant is held in place by one or two conductive surgical tacks [7, 10], and if the eye retains movement after surgery, the stimulator may move or partially lift over time because of the mobility of the eye. Lift-off allows a thin, conductive, film of vitreous humor to exist between the electrodes and the retinal surface, causing currents to have a path of smaller resistance toward the current return than going through the retina, where we intend to direct the charges. Because of the proximity to delicate retinal tissue, and the ability of the eye to change curvature, epiretinal stimulators are often encapsulated in soft, flexible materials [6]. This makes achieving and keeping a perfect contact between the electrode array and the retina even more challenging

A set of five simulations were performed to help understand the effect of lift-off in GCL current density magnitude for this stimulator, considering 100  $\mu m$  diameter platinum electrodes placed in a  $5 \times 5$  array configuration, separated 200  $\mu m$  between neighboring electrode centers, and considering lift-off values from 0  $\mu m$  (perfect contact) to 50  $\mu m$ , in 10  $\mu m$  intervals. For each case, the current density magnitude at the GCL under the center electrode was tabulated and reported in Table 4.3.

Table 4.3: Effect of lift-off on GCL current density magnitude for  $5 \times 5$  electrode array of 100  $\mu m$  electrodes. Values taken under the central electrode, all electrodes active, injecting 100  $\mu A$  each.

Lift-off ( $\mu m$ )	J ( $A \cdot m^{-2}$ )
0	4314.34
10	480.55
20	277.31
30	199.55
40	156.07
50	128.28

Figure 4.9 shows the effect of lift-off on the current density magnitude at the GCL, taken from under the central electrode of the array. Values under the other electrodes are relatively close. Larger values of lift-off cause significantly lower current densities, and tend to amalgamate the area of stimulation of electrodes into an undifferentiated zone.

To characterize the general effect of lift-off on GCL currents for this configuration, the values documented in Table 4.3 were curve-fitted, and scaled by the injected current. The resulting current density magnitude variation as a function of lift-off for this particular configuration is shown in Figure 4.9.

Assuming an even charge injection for all electrodes is desirable, the conclusion for this set of simulations is that in epiretinal configurations, it is critical for the stimulator array to conform to the curvature of the eye. While a smaller lift-off will make the implant more power efficient for the same amount of charge injected in the retinal tissue, a larger gap between the retinal surface and the stimulator will make the effect of small variations of the lift-off value for different electrodes smaller. A larger lift-off will also result in less defined stimulation areas at the GCL. If the curvature of the prosthesis does not follow the surface of the retina, electrodes will not achieve an even charge injection unless the current injected by each individual electrode is adjusted using a current density magnitude versus lift-off curve adequate for the device geometry.

### 4.3.2 Effect of Electrode Diameter

Electrode diameter affects the size of the area affected by stimulation, and is relevant to the safety of the implant. In the short term, it affects the peak current density for a target amount of charge injection, as current density is inversely proportional to the section of the electrode. In the long term, for metallic electrodes, having a larger current density will likely imply a higher amount of faradaic charge injection and introduce new chemical species at the electrode-electrolyte interface [2, 52]. This process is toxic for the living tissue, detrimental for the longevity of the metal electrodes, and reduces the efficiency of the electrical stimulation over time [2].

A set of five simulations were performed using the multiresolution admittance method, and the results for each case tabulated in Table 4.4. The values from Table 4.4 were curve-fitted to better understand the relation between electrode size and current density magnitude at the GCL under the central electrode for this configuration, and plotted in Figure 4.10. As expected, if all other parameters are the same, smaller electrodes resulted in higher current density magnitudes at the GCL. It was also observed that using even the largest diameter electrodes, the individual spots under each active electrode were clearly differentiated.

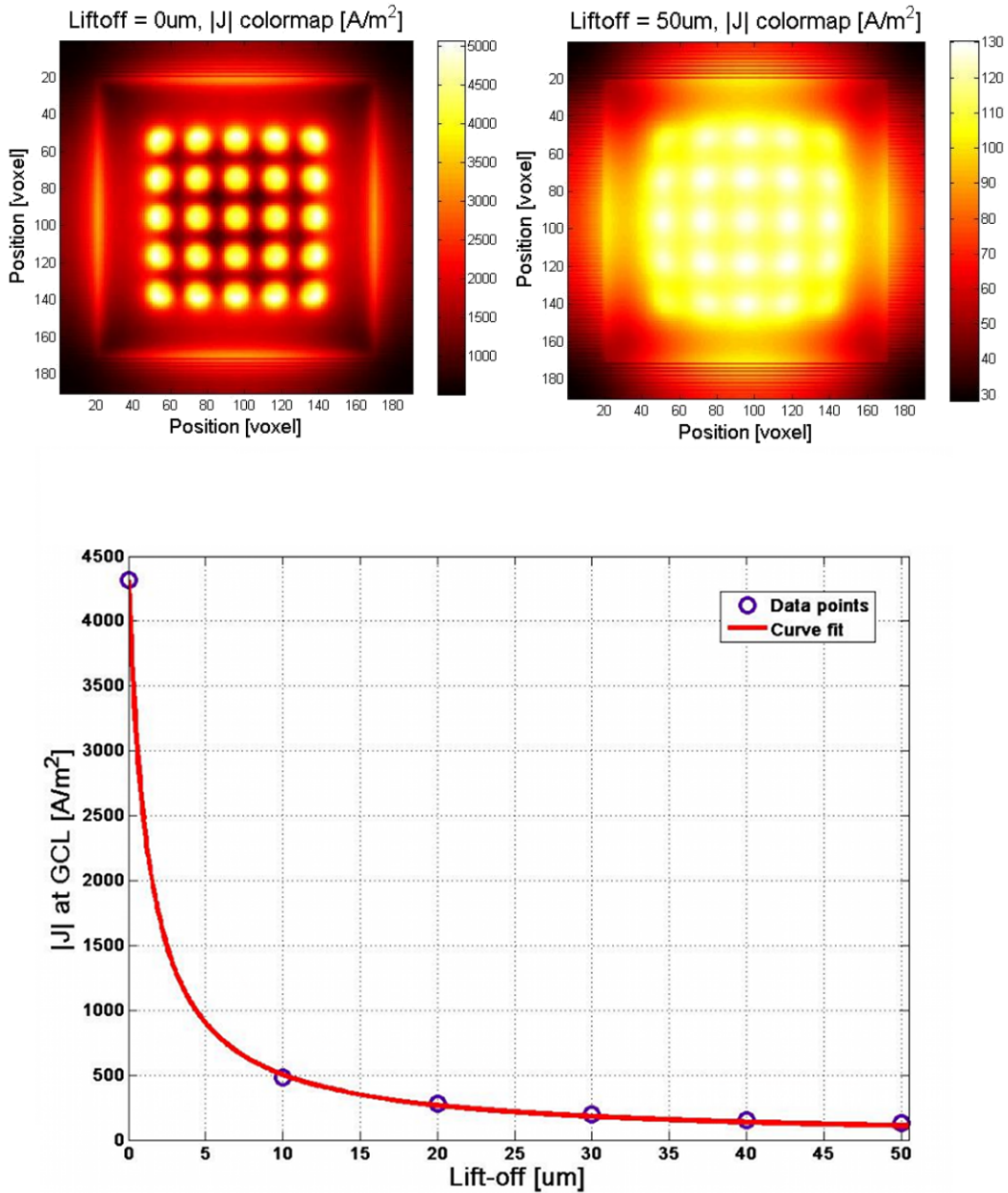


Figure 4.9: Effect of lift-off in current density magnitude at GCL. Current density magnitude for electrode array in perfect contact with retinal surface (*Top Left*). Current density magnitude for electrode array lifted  $50 \mu\text{m}$  from retinal surface (*Top Right*). Current density magnitude as a function of lift-off for  $100 \mu\text{m}$  diameter electrodes. Value of current density magnitude taken in GCL at center of central electrode of array. All electrodes active, each injecting  $100 \mu\text{A}$  (*Bottom*).

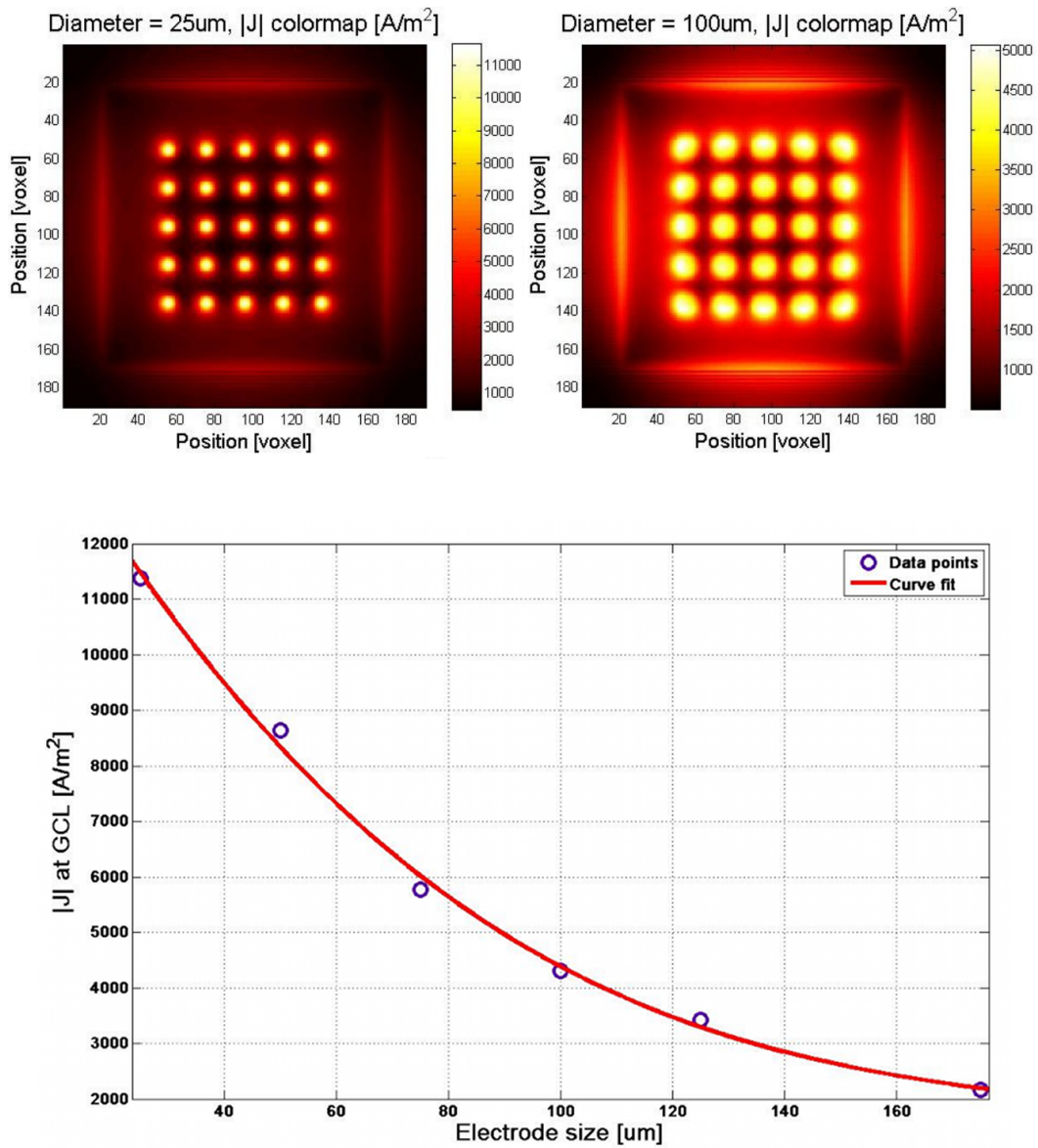


Figure 4.10: Effect of electrode diameter on current density magnitude at GCL. Current density as a function of electrode diameter. Value of current density taken in GCL at center of central electrode of array. All electrodes active, each injecting  $100 \mu A$ .



Table 4.4: Effect of electrode diameter in GCL current density y magnitude for  $5 \times 5$  electrode array. Values taken under the central electrode, all electrodes active, injecting  $100 \mu A$  each..

Diameter ( $\mu m$ )	J ( $A \cdot m^{-2}$ )
25	11372.90
50	8634.51
75	5768.58
100	4314.34
125	3428.61
175	2172.18

### 4.3.3 Effect of Electrode Current Return Placement

When the current return is close to the stimulating electrodes, its placement plays an important role on the distribution of injected charges. Many parameters affect the outcome in this case, making it hard to characterize. Among the most important are current return position with respect to the active stimulating electrode, geometry of near-by tissue structures, and the shape of the current return. This variation is not as pronounced when the current return is far away from the stimulator; this was expected as that case more accurately approximates monopolar stimulation. To qualitatively illustrate the kind of variation in current density magnitude we could expect depending on the current return configuration for current return placement close to the stimulating electrode array, two simulations of a high-density 1024 electrode stimulator were performed, the first using a disc shaped current return close to one of the corners of the insulating backing of the electrode array, and the second using a long conductive bar spanning one entire edge of the stimulator pad. Both models considered a laminar model of the retina. Resulting current densities at GCL are shown as a color plot in Figure 4.11.

It can be observed that even when all active electrodes are injecting the same amount of current, the current densities at the GCL greatly vary for each case, and are uneven for neighboring electrodes. Partly because of this effect, the current return in the actual implants is positioned as far as possible from the actual stimulator.

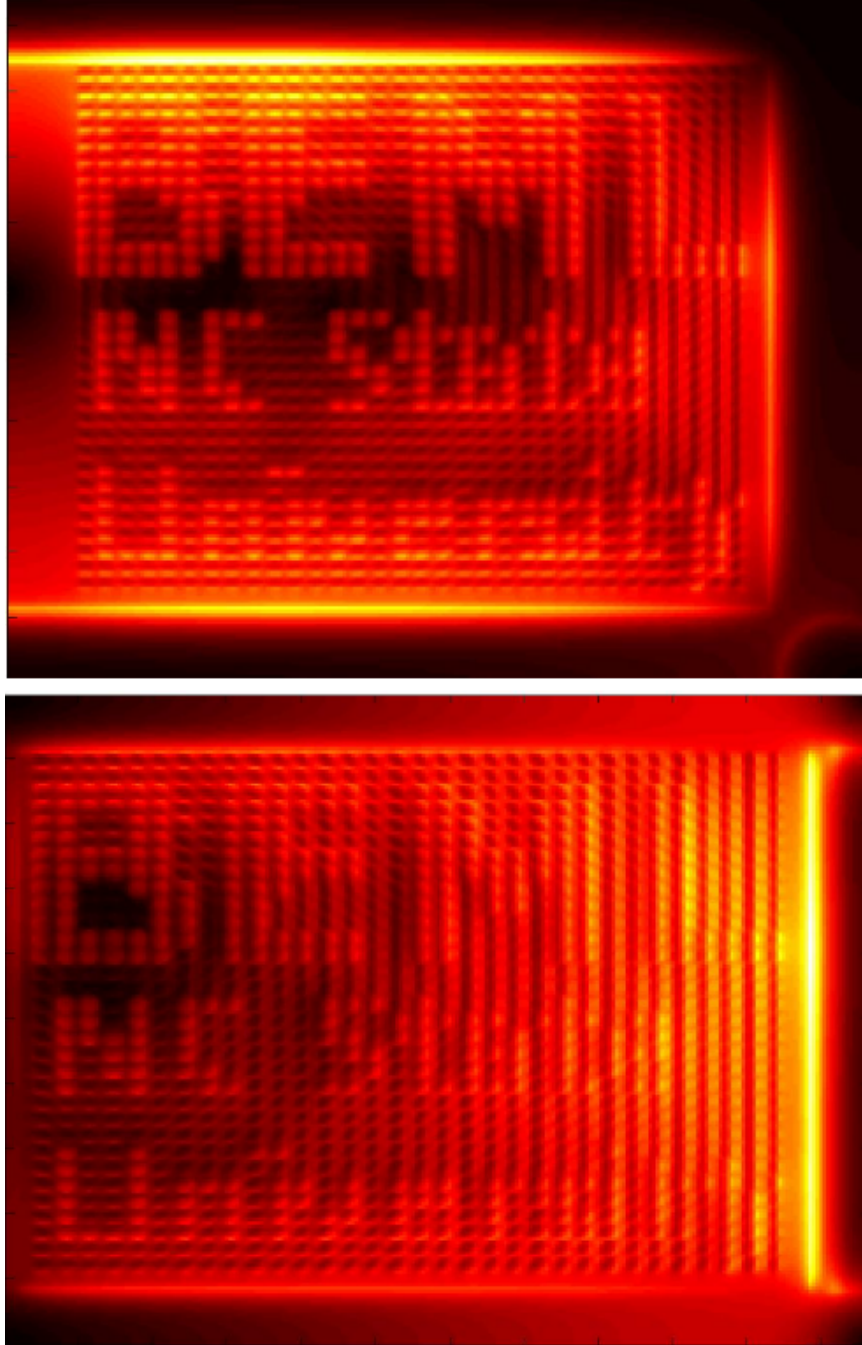


Figure 4.11: Effect of current return placement on current density magnitude at GCL, for electrode arrays having 1024 electrodes. Active electrodes spell pattern reading "BEML NC State University". All active electrodes are injecting the same amount of current in both plots. Disc shaped current return at the lower right corner (*Top*) produces higher current densities as the top and bottom of electrode array. Bar shaped current return at the right of array (*Bottom*) produces higher current densities on the half of the array closer to the current return.

## Chapter 5

# Modeling Cellular Lysis In Skeletal Muscle due to Electric Shock <sup>†</sup>

### 5.1 Abstract

High-voltage electrical trauma frequently results in injury patterns that cannot be completely attributed to injury mediated by heat. An electrical injury model describing cellular lysis damage caused by supraphysiological electric fields was derived and used to evaluate the effects of high-voltage electric shock on the skeletal muscle of a human upper limb, in a configuration that simulates hand-to-hand contact. The resulting current through the arm and the electric field inside the tissue were calculated using a multi-resolution variant of the admittance method and a millimeter resolution anatomically correct model of a human upper limb. The injury model was used to estimate progressive damage of skeletal muscle in the arm. Values for the current through the arm and the upper limb impedance are reported as well.

---

<sup>†</sup> From Carlos J. Cela, Raphael C. Lee, and Gianluca Lazzi, *Modeling Cellular Lysis In Skeletal Muscle due to Electric Shock*, to be submitted for publication.

## 5.2 Introduction

High-voltage electrical trauma frequently results in injury patterns involving selective destruction of muscle and nerve tissue [18]. These patterns cannot be completely attributed to injury mediated by heat. It has been reported in the literature that besides thermal injury caused by Joule heating, cellular membrane pore formation leading to cellular membrane rupture and direct electroconformational denaturation of macromolecules, such as proteins, are active tissue-damaging mechanisms in the presence of supra-physiological electric fields [19, 20].

Among high-voltage electric shock accidental exposures, hand-to-hand circuit paths count among the most common occurrences, and the most sensitive tissues to damage are skeletal muscle and nerve. Further, there is evidence that electrical injury in muscle tissue by pore formation in cellular walls affects the conductivity of tissue [19].

It was of interest, then, to model the effect of a hand-to-hand high-voltage electric shock on human skeletal muscle conductivity. We focus on modeling the effects of cellular membrane rupture caused by an externally applied electric field, and how this affects tissue conductivity. When low-frequency electric shocks are applied to skeletal muscle, the electrical current is effectively shielded from the cytoplasmic fluid by the cellular membranes. Because the presence of cells in bodily tissue diminishes the extracellular volume available for ionic currents, and the cellular membrane is comparatively more resistive, tissue with tightly packed cells is less conductive. When cell membranes rupture due to the action of supra-physiological electric fields, the cytoplasmic fluid is in direct electrical contact with extracellular fluid and available to conduct current, increasing the overall conductivity of the affected tissue. This effect was experimentally measured and reported by Bhatt in [19].

In this work, a numerical model for muscle injury from electrical shock was derived from available experimental data and used to evaluate the effects of a one second 10kV electric shock on skeletal muscle of a human upper limb, in a configuration that simulates hand-to-hand contact. The arrangement shown in Figure 5.1 was used to approximate this case. Resulting currents and electric field inside the tissue due to the applied shock were calculated using the multiresolution variant of the admittance method described in Chapter 3 and a millimeter resolution anatomically correct model of a human upper limb [45]. The model considered dielectric properties of skeletal muscle, bone, fat, skin, and 14 other tissues.

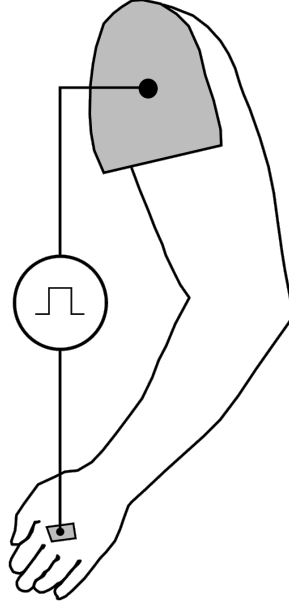


Figure 5.1: Configuration used for calculating electric field inside upper limb. Current was injected into  $5\text{cm}^2$  hand electrode, and current return consisted of a metal plate covering the entire surface exposed when arm was sectioned from body. A pulsed source injected  $10\text{ ms}$  pulses having an amplitude of  $4.5\text{ kV}$ .

### 5.3 Electric Injury Model for Cellular Lysis

Consider a sample of muscle tissue positioned between two electrodes as shown in Figure 5.2, having a length  $L$  and a cross-section  $A$ . The sample is subjected to a longitudinal pulsed electric field generated by  $V$ . Electrically, we model the conductance of a single cell as  $\gamma_c$  if the cell is intact and as  $\gamma_l$  if the cell is lysed.

Initially, the sample has  $N$  intact cells. With each delivered shock a fraction  $\varepsilon$  of all remaining intact cells is lysed. In our approximation, the conductance of the lysed cells is in parallel with the conductance of the remaining intact cells, as depicted in Figure 5.3. After  $i$  shocks are delivered, assuming that  $\varepsilon$  remains constant through the experiment, a number  $N(1 - \varepsilon)^i$  of cells will remain intact (Table 5.1), and the remaining  $L_i$  cells will be lysed by action of the electric field (5.1).

$$L_i = N - N(1 - \varepsilon)^i \quad (5.1)$$

The conductance  $\gamma_i$  of the sample after  $i$  pulses can be expressed as the conductance

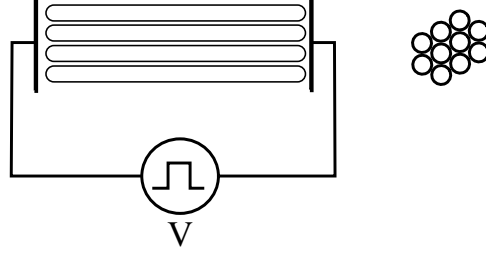


Figure 5.2: Diagram of injury model setup. Muscle tissue sample is exposed to a pulsed electric field generated by voltage source  $V$  (*Left*). Cross-section of tissue sample between electrodes (*Right*)

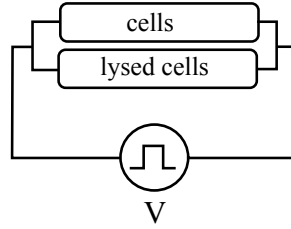


Figure 5.3: Conductance when considering intact and lysed cells.

of the intact cells in parallel with the conductance of the lysed cells. This approach will work if we consider that eventually all cells in our sample will be lysed by the action of the electric field; however, this turns out not to be the case. If we observe the experimental measurements in Figure 5.4, it can be seen that the curves of maximum normalized conductivity fraction converge to higher conductivity values when stronger electric fields are used for the pulses. This suggests that regardless of how many pulses are applied at low field strengths, not all cells in the sample will lyse. To correct for this effect, a parameter  $\alpha_l$ , dependent of the electric field magnitude, is introduced, affecting the maximum apparent conductivity of the sample. The overall conductivity of the tissue sample after  $i$  pulses can then be expressed as (5.2).

$$\gamma_i = (N - L_i) \gamma_c + L_i \alpha_l \gamma_l \quad (5.2)$$

Using (5.1), we can express (5.2) as (5.3).

$$\gamma_i = N \left( \alpha_l \gamma_l + (1 - \varepsilon)^i (\gamma_c - \alpha_l \gamma_l) \right) \quad (5.3)$$

While the conductance values can be measured experimentally,  $\varepsilon$  and  $\alpha_l$  characterize

Table 5.1: Calculation of remaining healthy cells after a given number of pulses, starting with  $N$  healthy cells, having a fraction  $\varepsilon$  of remaining healthy cells lysed every pulse. The general expression (bottom, left) is obtained using mathematical induction.

Number of electric pulses	Number of healthy cells remaining	General form
0	$N$	$N(1 - \varepsilon)^0$
1	$N - N\varepsilon$	$N(1 - \varepsilon)^1$
2	$(N - N\varepsilon) - (N - N\varepsilon)\varepsilon$	$N(1 - \varepsilon)^2$
...		
$i$		$N(1 - \varepsilon)^i$

the effects of multiple factors in the model, including cell history, temperature, electric field strength, electric pulse duration, etc, and must be derived by fitting experimental data. In addition, while (5.2) is intuitive, for purposes of numerical modeling it is desirable to have a formulation independent of the form factor of the tissue sample, that is, to consider conductivities instead of conductances. Using analogous reasoning to what we used for (5.3), but considering conductivities instead of conductances and lysed volume fraction per pulse instead of number of cells lysed per pulse we can express the tissue conductivity as (5.4).

$$\sigma_i = \beta_l \sigma_l + (1 - \delta)^i (\sigma_c - \beta_l \sigma_l) \quad (5.4)$$

In (5.4),  $\sigma_c$  is the conductivity of intact tissue,  $\sigma_l$  is the conductivity of tissue having all cells lysed,  $\beta_l$  is the analogous factor of  $\alpha_l$ ,  $\sigma_i$  is the conductivity of the tissue after  $i$  electric shocks have been applied, and  $\delta$  is the fraction of volume lysed by a single pulse, which corresponds to  $\varepsilon$  in (5.3). The intact and lysed tissue conductivities are related to their respective conductance values by (5.5) and (5.6) respectively.

$$\sigma_c = \left( \frac{N \cdot L}{A_c} \right) \gamma_c \quad (5.5)$$

$$\sigma_l = \left( \frac{N \cdot L}{A_l} \right) \frac{\alpha_l}{\beta_l} \gamma_l \quad (5.6)$$

Equation (5.5) considers a tissue sample having all cells intact, a uniform cross-section of  $A_c$ , and a length  $L$ . Equation (5.6) considers all cells in the tissue sample to be lysed, a uniform cross-section  $A_l$  and a length  $L$ . If both  $\sigma_c$  and  $\sigma_l$  are the extreme values for conductance of the same tissue sample,  $A_c$  and  $A_l$  will have the same value,  $\alpha_l$  and  $\beta_l$  will have the same value, and by dividing (5.6) by (5.5) we can see that the fractional variation of conductance with tissue injury equals the fractional variation of conductivity, as shown in (5.7). This is helpful in which it allows us to use normalized conductance experimental values to obtain normalized conductivity values of tissue.

$$\frac{\sigma_l}{\sigma_c} = \frac{\gamma_l}{\gamma_c} \quad (5.7)$$

Following logic similar to what we used for (5.1) before, the lysed volume fraction  $K_i$  can be computed as (5.11).

$$K_i = 1 - H_i \quad (5.8)$$

where  $H_i$  is the volume fraction of tissue occupied by intact cells after  $i$  pulses, and can be expressed using (5.9).

$$H_i = (1 - \delta)^i \quad (5.9)$$

The specific impedance of the tissue  $z_i$  after  $i$  pulses can now be expressed as (5.10) .

$$z_i = \frac{1}{\beta_l \sigma_l + H_i (\sigma_c - \beta_l \sigma_l)} \quad (5.10)$$

Using (5.4), (5.8), and (5.9) we can now express the total lysed volume fraction  $K_i$  as a function of the tissue conductivity  $\sigma_i$  (5.11).

$$K_i = 1 - \left( \frac{\sigma_i - \sigma_l}{\sigma_c - \sigma_l} \right) \quad (5.11)$$

Note that  $\beta_l$  is purposely not included in (5.11), as we intend  $K_i$  to refer the total lysed volume fraction to maximum conductivity (i.e. 100% of cells lysed), independently of the maximum fraction of cells lysed for the applied electric field magnitude.



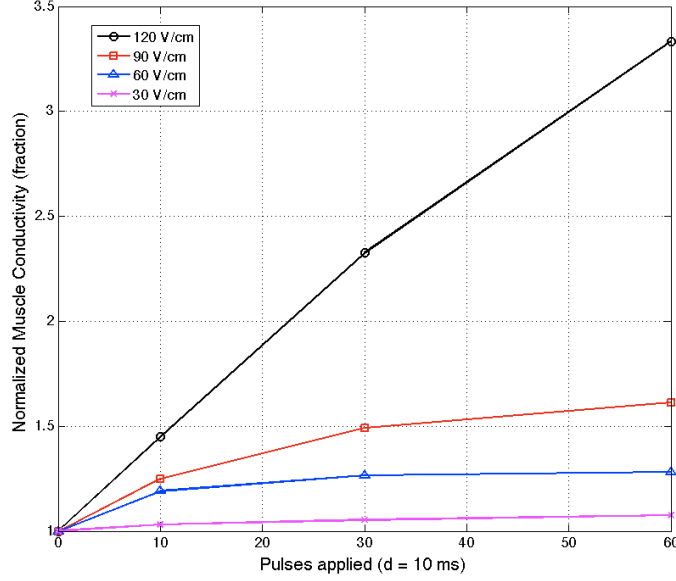


Figure 5.4: Normalized conductivity fraction variation in biceps femoris of Sprague-Dawley rats as 10ms electric pulses are applied, for different electric field magnitudes. Data points calculated by applying (5.12) to experimental data reports by Bhatt *et al* [19]

## 5.4 Experimental Data Fitting

In 1990, Bhatt *et al* produced experimental data on normalized impedance variation as a function of number, duration and strength of electric pulses applied to muscle samples from biceps femoris from Sprague-Dawley rats [19]. Our goal was to use this data to predict similar variations in human muscle by means of numerical simulations. In order to arrange the data in an appropriate format for numerical simulations, (5.12) was used to convert the percent normalized impedance  $z_{percent}$  to a normalized conductivity fraction, as shown in Figure 5.4.

$$\frac{\sigma_i}{\sigma_c} = \frac{100}{z_{percent}} \quad (5.12)$$

To obtain a general expression of the conductivity after a number  $i$  of electric pulses has been applied  $\sigma_i$ , the data points from Figure 5.4 were fitted to equation (5.4) using non-linear least squares fitting. Considering a normalized conductivity of  $\sigma_c = 1$  for intact cells, this resulted in values of  $\delta$  and  $\beta_l$  for each strength of electric field, as reported in

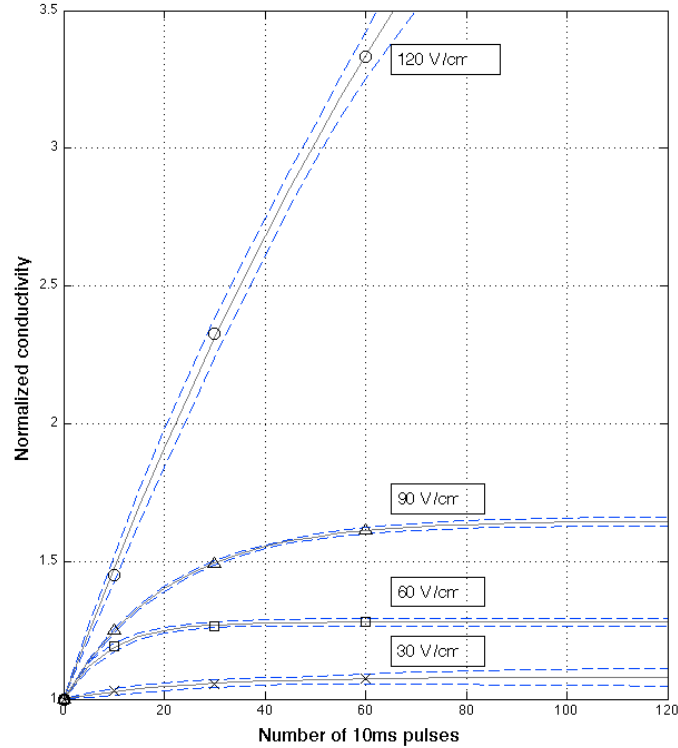


Figure 5.5: Normalized conductivity fraction variation as a function of number of pulses applied, obtained by fitting (5.4) to experimental data from [19] (data points marked with geometrical shapes in figure). Pointed lines show upper and lower 95% confidence bounds for the fitting.

Table 5.2. For purposes of our approximation, it was considered that an electric field having a magnitude of  $30 \text{ V} \cdot \text{m}^{-1}$  or smaller would not damage intact cells.

Since  $\delta$  and  $\beta_l$  vary with the strength of the electric field, the values from Table 5.2 were fitted to obtain the intermediate values as needed. The resulting equations are (5.13) and (5.14). Assuming pulses of 10 ms duration and equal magnitude, and tissue conductivities normalized so  $\sigma_c = 1$ , the resulting normalized conductivity  $\sigma_i$  after a number of pulses have been applied can be calculated in two steps: First the corresponding values for  $\delta$  and  $\beta_l$  are calculated using (5.13) and (5.14). Second, (5.4) is used to calculate the tissue conductivity after the pulses have been applied. Figure 5.5 shows conductivity curves resulting from the fitted functions below for a range of voltages.

$$\delta = 0.7441 e^{-0.03214 |E|} \quad (5.13)$$

Table 5.2: Values for 10ms pulses.  $|\vec{E}|$  is expressed in  $V \cdot cm^{-1}$ .  $\beta_l$  and  $\delta$  are adimensional.

$ \vec{E} $	$\beta_l$	$\delta$
30	0.28827	-
60	0.34107	0.10710
90	0.43947	0.04704
120	1.87520	0.008134

$$\beta_l = \frac{\sigma_c}{\sigma_l} (0.9163 e^{0.005507 |E|} + 2.949 \times 10^{-6} e^{0.1199 |E|}) \quad (5.14)$$

In equations (5.13) and (5.14),  $|E|$  represents the magnitude of the longitudinal electric field that the muscle cells are exposed to in every pulse. For purposes of our numerical simulation, we considered two extreme values for muscle conductivity:  $\sigma_c = 0.4 S \cdot cm^{-1}$  [16] when all cells are intact, and  $\sigma_l = 1.5 S \cdot cm^{-1}$ , the conductivity of body fluid [50], when all cells are lysed. When normalized,  $\sigma_c = 1$  and  $\sigma_l = 3.75$ ; further, the value of  $\sigma_i$  is never taken as larger than the  $\sigma_l$  value, as we interpret that all cells are lysed the moment that expression (5.4) reaches the  $\sigma_l$  value. Using (5.11), Figure 5.6 shows the total lysed fraction in muscle as a function of its conductivity.

## 5.5 3-D Multiresolution Admittance Method

In order to calculate electric injury by cellular lysis inside a human arm, we have first to determine the electric field strength. The multiresolution admittance method described in Chapter 3 was used to determine the electric field strength for each point in the skeletal muscle of the arm.

## 5.6 Numerical Modeling and Simulation

The size of the model was  $636 \times 315 \times 302$  voxels, and it considered the tissues and conductivities reported in Table 5.3. Once the multiresolution algorithm was applied, considering  $M = 4$ , the voxel count dropped to 7.4% of the original size, from over 60 million to under 5 million voxels.

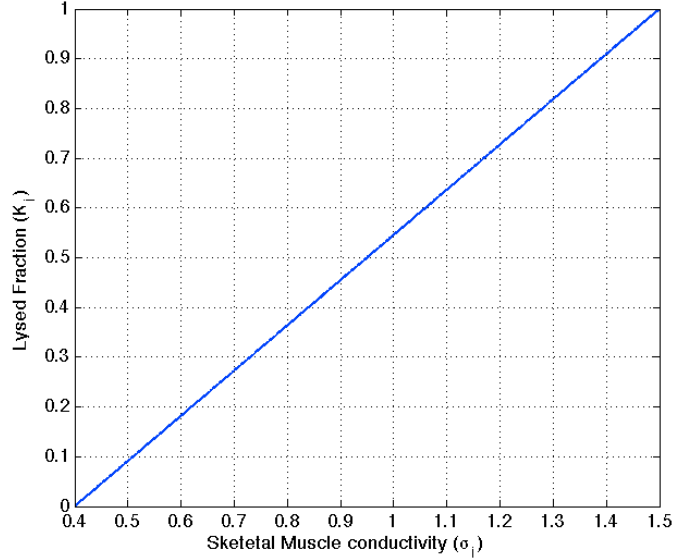


Figure 5.6: Lysed fraction  $K_i$  as a function of muscle conductivity  $\sigma_i$ , for the ranges used during the simulation.

The skin-electrode interface conductivity was calculated considering a  $1 \mu F \cdot cm^{-2}$  contact capacitance, perfect electrode contact, and half of the current conduction and half displacement [16]. The skin immediately under the electrode was removed; the hand electrode was in direct contact with muscle and fat. This was done to simulate reported effects of the underlying skin evaporating almost immediately upon high-voltage contact [16]. Other conductivity values considered are values reported for 60 Hz in [16], [53] and [4]. A 1 A DC current source connected to a  $5 cm^2$  metallic electrode was positioned in the palm of the hand, having its current return at a large metallic plate completely covering the tissue exposed where the arm was sectioned from the body, as depicted in Figure 5.1. Since the injected current was 1 A, the resulting voltages represent the numerical value of the impedance with respect to the current return plate at the shoulder. This resulted in a total arm impedance between the metal side of both electrodes of  $814\Omega$ , considering the metal-tissue interface, and an impedance of  $550\Omega$  between the tissue side of both electrodes, without considering the interface.

To simulate the effect of a 60 Hz, 10 kV hand-to-hand contact, the current injection was scaled so it resulted in 4.5 kV applied between the hand electrode and the current return plate at the shoulder. This resulted in a total current of 5.53 A circulating through the arm. The magnitude of the electric field in the model was then calculated from the

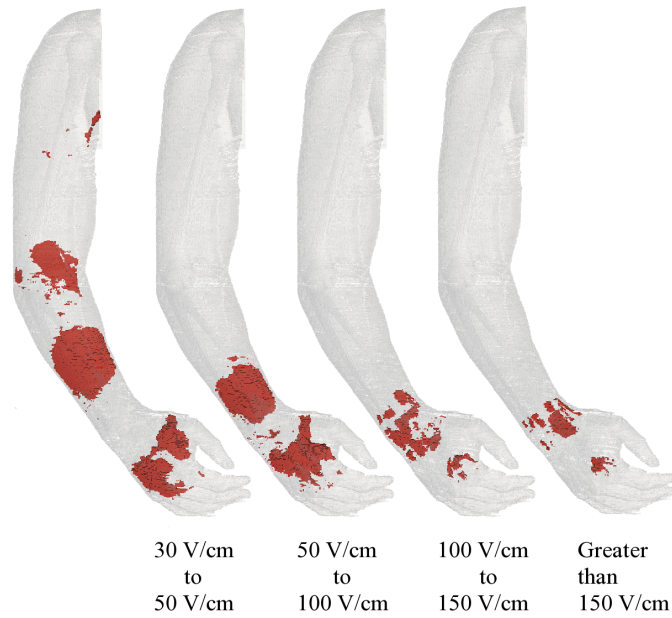


Figure 5.7: Electric field magnitudes resulting from a 4.5 kV shock. From left to right, each diagram shows the volumes inside the arm having increasing electric field strength.

electric potentials. The regions of the arm having electric fields with a magnitude large enough to cause cellular lysis as a result of the applied pulses are shown in Figure 5.7. The maximum electric field resulting from this configuration was in excess  $400 \text{ V} \cdot \text{cm}^{-1}$ , at the interface between the hand electrode and the tissue.

Assuming that cellular lysis is roughly proportional to the total energy delivered by the pulses, the 4.5 kV, 1 s, 60 Hz, sinusoidal, high-voltage electric shock was modeled as 100 rectangular pulses, each of them having a duration of 10 ms and an amplitude of 4.5 kV.

$\beta_l$  and  $\delta$  were then determined for each voxel in the model, using the calculated electric field magnitude and equations (5.13) and (5.14). The resulting conductivity after a number of pulses was then calculated using (5.4), and the fraction of lysed cells determined using (Figure 5.6). The resulting injury patterns are presented in Figure 5.8 and Figure 5.9.

Table 5.3: Tissue Conductivities

Material / Tissue	Conductivity ( $S \cdot m^{-1}$ )
Air	$1.000 \times 10^{-7}$
Metal	$1.000 \times 10^6$
Body fluid	1.500
Fat	$5.000 \times 10^{-2}$
Lymph	$5.217 \times 10^{-1}$
Nail	$2.006 \times 10^{-2}$
Nerve	$2.765 \times 10^{-2}$
Muscle (intact)	$4.000 \times 10^{-1}$
Muscle (lysed)	(as Body fluid)
Glands	$5.217 \times 10^{-1}$
Blood vessel	$2.648 \times 10^{-1}$
Bone (cortical)	$1.000 \times 10^{-2}$
Cartilage	$1.717 \times 10^{-1}$
Ligaments (muscle)	$4.000 \times 10^{-1}$
Skin (dry)	$3.800 \times 10^{-4}$
Blood	$7.000 \times 10^{-1}$
Bone marrow	$1.699 \times 10^{-3}$
Bone (cancellous)	$1.000 \times 10^{-2}$
Skin-Electrode Interface	$7.540 \times 10^{-3}$

## 5.7 Discussion

The electric injury model parameter  $\beta_l$  affects the maximum amount of damage that a set of pulses of a given electric field magnitude can cause.  $\delta$  affects how much of that damage is delivered with each pulse. The combined effect of  $\beta_l$  and  $\delta$  for a given field strength can be clearly appreciated in Figure 5.8 and Figure 5.9; while the relatively lower fields caused faster but limited amount of lysis in the middle forearm, the higher field strength on the distal forearm caused more damage at a slower rate. The time-sequence of damage in Figure 5.9 shows that in this case, muscle damage by cellular lysis happens in the first half second of exposure.

It is interesting to notice the geometry of the lysed areas in Figure 5.9. The overall tendency is for the current density to increase towards the distal portion of the forearm, since the cross-section of the arm is smaller. This causes higher electric field magnitudes



Figure 5.8: Progressive damage (left to right) in muscle and tendon by cell lysis due to applied electric shock.

as we get closer to the wrist, as illustrated in Fig. 5.7.

While volumes of tissue allow for an even spread of current, constrictions in the current flow cause local increases of the electric field strength, and consequently, increased local damage. Several of these cases can be observed in Figure 5.8 and Figure 5.9. For instance, the inside fold of the elbow presents a region showing cellular lysis; this is likely caused by the slight bend of the arm in the model making the anterior distal region of the upper arm the shortest path for current to flow through. The same effect is noticeable in the axilla. These injury patterns suggest that tissue damage distribution may depend of the position of the arm during exposure. In the wrist, the restriction to current flow is given by the larger amount of bone in proportion to muscle tissue; because bone is relatively less conductive, this causes higher local current densities inside other tissues, resulting in stronger electric fields and significantly higher damage.

The multiresolution algorithm described in Chapter 3 proved to be valuable tool to reduce the size of the model, an hence computational overhead, by over 90%, while



Figure 5.9: Progressive damage (left to right) in muscle and tendon by cell lysis due to applied electric shock.

keeping an acceptable numerical error.



# Chapter 6

## Conclusion

Accurate modeling of bioelectromagnetic problems present a distinctive set of challenges. Models have complex geometrical features and their size tends to be large compared to the minimum feature size. Dielectric properties of biological materials tend to be anisotropic and vary with frequency, temperature, electric field applied, and current density going through tissue. In the particular case of having metal in contact with living tissue, as in the case of medical implants, there is a set of local electrochemical reactions that affect the interaction.

A formulation of the admittance method with potential to address these challenges has been introduced. The multiresolution scheme presented in Chapter 3 addresses the concerns regarding treatment of large problem spaces having detailed, small features, by reducing the voxel count five to ten fold in typical biological models. This speeds up computations and drastically reduces memory footprint of the numerical codes. For certain particular problems, for instance, to find the low frequency impedance between two electrodes in a 1 *mm* resolution of a full human body, the multiresolution admittance method proved to be over two orders of magnitude faster than FDTD, while providing comparably accurate results [40].

An important advantage of the admittance method is that since the model is represented in terms of a lumped element electrical network, new electrical components can be arbitrarily included in the network to account for electromagnetic effects not present in the original model. This is particularly useful in the context of medical devices that use implanted electrodes, as complex electrochemical interactions between electrodes and electrolytes can be modeled using electrical networks [2, 32].

Applications of the proposed method to implanted devices were documented. These by no means exhaust the capabilities of the multiresolution admittance method.

## References

- [1] M. Sadiku. *Numerical Techniques in Electromagnetics*. CRC Press, second edition, 2000.
- [2] S. B. Brummer and L. S. Roblee. Criteria for selecting electrodes for electrical stimulation: Theoretical and practical considerations. *Annals of the New York Academy of Sciences*, 405:159–171, 1983.
- [3] C. Gabriel, S. Gabriel, and E. Corthout. The dielectric properties of biological tissues: I. literature survey. *Phys. Med. Biol.*, 41:2231–2249, 1996.
- [4] L. A. Geddes and L. E. Baker. The specific resistance of biological material - a compendium of data for the biomedical engineer and physiologist. *Med. and Biol. Engng.*, 5:271–293, 1967.
- [5] M. S. Humayun, E. De Juan Jr., J. D. Weiland, G. Dagnelie, S. Katona, R. Greenberg, and S. Suzuki. Pattern electrical stimulation of the human retina. *Vision Research*, 39, 1999.
- [6] JD Weiland, WT Liu, and MS Humayun. Retinal prosthesis. *Annual Review of Biomedical Engineering*, 7:361–401, 2005.
- [7] Mark S. Humayun, James D. Weiland, Gildo Y. Fujii, Robert Greenberg, Richard Williamson, Jim Little, Brian Mech, Valerie Cimmarusti, Gretchen Van Boemel, Gislin Dagnelie, and Eugene de Juan. Visual perception in a blind subject with a chronic microelectronic retinal prosthesis. *Vision Research*, 43(24):2573 – 2581, 2003.
- [8] Daniel Palanker, Alexander Vankov, Phil Huie, and Stephen Baccus. Design of a high-resolution optoelectronic retinal prosthesis. *J. Neural Eng.*, 2(1):S105–S120, 2005.
- [9] Douglas B. Shire, Shawn K. Kelly, Jinghua Chen, Patrick Doyle, Marcus D. Gingerich, Stuart F. Cogan, William A. Drohan, Oscar Mendoza, Luke Theogarajan, John L. Wyatt, and Joseph F. Rizzo. Development and implantation of a minimally invasive wireless subretinal neurostimulator. *IEEE Trans. Biomed. Eng.*, 56(10), 2009.
- [10] Gernot Roessler, Thomas Laube, Claudia Brockmann, Thomas Kirschkamp, Babac Mazinani, Michael Goertz, Christian Koch, Ingo Krisch, Bernd Sellhaus, Hoc Khiem Trieu, Joachim Weis, Norbert Bornfeld, Harald Roethgen, Arthur Messner, Wilfried Mokwa, and Peter Walter. Implantation and explantation of a wireless epiretinal retina implant device: Observations during the epiret3 prospective clinical trial. *Investigative Ophthalmology and Visual Science*, 50(6):3003–3008, June 2009.

- [11] H. Wassle and B. B. Boycott. Functional architecture of the mammalian retina. *Physiological Reviews*, 71(2), April 1991.
- [12] R. W. Rodieck. The primate retina. *Comp. Primate Biol.*, 4(203-278), 1988.
- [13] Frank Rattay. Analysis of models for external stimulation of axons. *IEEE Trans. Biomed. Eng.*, 33(10):974–7, 1986.
- [14] Bryan W. Jones and Robert E. Marc. Retinal remodeling during retinal degeneration. *Experimental Eye Research*, 81:123–137, 2005.
- [15] Robert E. Marc, Bryan W. Jones, James R. Anderson, Krista Kinard, David W. Marshak, John H. Wilson, Theodore Wensel, and Robert J. Lucas. Neural reprogramming in retinal degeneration. *Investigative Ophthalmology and Visual Science*, 48(7), 2007.
- [16] B. I. Tropea and R. C. Lee. Thermal injury kinetics in thermal injury kinetics in electrical trauma. *J. Biomech. Eng.*, 114, 1992.
- [17] R. C. Lee and W. Dougherty. Electrical injury: Mechanisms, manifestations, and therapy. *IEEE Transactions on Dielectric and Electrical Insulation*, 10(5):810–819, October 2003.
- [18] D. C. Gaylor, K Prakah-Asante, and R. C. Lee. Significance of cell size and tissue structure in electrical trauma. *J. Theor. Biol.*, 133:223–237, 1988.
- [19] Deepak L. Bhatt, Diane C. Gaylor, and Raphael C. Lee. Rhabdomyolysis due to pulsed electric fields. *Plastic and Reconstructive Surgery*, 86(1), 1990.
- [20] Diane C. Gaylor. *Physical Mechanisms of Cellular Injury in Electrical Trauma*. PhD thesis, M.I.T., 1989.
- [21] R. C. Lee. Physical mechanisms of tissue injury in electric trauma. *IEEE Trans. Educ.*, 34(3):223–230, August 1991.
- [22] R. C. Lee, D. J. Zhang, and J. Hannig. Biophysical injury mechanisms in electrical shock trauma. *Annual Review of Biomedical Engineering*, 2, 2000.
- [23] A. Thom and C. J. Apelt. *Field Computations in Engineering and Physics*. Van Nostrand Company, 1961.
- [24] Kane S. Yee. Numerical solution of initial boundary value problems involving maxwell's equations in isotropic media. *IEEE Trans. Antennas Propag.*, AP-14(3), 1966.

- [25] Christopher E. Reuter, Rose M. Joseph, Eric T. Thiele, Daniel s. Katz, and Allen Taflove. Ultrawideband absorbing boundary condition for termination of waveguiding structures in fd-td simulations. *IEEE Microwave and Guided Wave Letters*, 4(10), 1994.
- [26] Jean Pierre Berenger. Numerical reflection from fdtd-pmls: A comparison of the split pml with the unsplit and cfs pmls. *IEEE Trans. Antennas Propag.*, 50(3), 2002.
- [27] Feng Liu and Stuart Crozier. A distributed equivalent magnetic current based fdtd method for the calculation of e-fields induced by gradient coils. *Journal of Magnetic Resonance*, 169:323–327, 2004.
- [28] Huawei Zhao, Stuart Crozier, and Feng Liu. Finite difference time domain (fdtd) method for modeling the effect of switched gradients on the human body in mri. *Magnetic Resonance in Medicine*, 48:1037–1042, 2002.
- [29] Trevor W. Dawson, J. De Moerloose, and Maria A. Stuchly. Comparison of magnetically induced elf fields in humans computed by fdtd and scalar potential fd codes. *ACES J.*, 11:63–71, 1996.
- [30] Trevor W Dawson, Kris Caputa, and Maria A Stuchly. A comparison of 60 hz uniform magnetic and electric induction in the human body. *Phys. Med. Biol.*, 42:2319–2329, 1997.
- [31] P. J. Dimbilow. Induced current densities from low-frequency magnetic fields in a 2 mm resolution, anatomically realistic model of the body. *Phys. Med. Biol.*, 43:221–230, 1998.
- [32] L. A. Geddes. Historical evolution of circuit models for the electrode-electrolyte interface. *Ann. Biomed. Eng.*, 25:1–14, 1997.
- [33] A. L. Hodgkin and A. F. Huxley. A quantitative description of membrane current and its application to conduction and excitation in nerve. *J. Physiol.*, 117, 1952.
- [34] D. W. Armitage, H. H. LeVeen, and R. Pethig. Radiofrequency-induced hyperthermia: Computer simulation of specific absorption rate distributions using realistic anatomical models. *Phys. Med. Biol.*, 28:31–42, 1983.
- [35] O. P. Gandhi, J. F. DeFord, and H. Kanai. Impedance method for calculation of power deposition patterns in magnetically induced hyperthermia. *IEEE Trans. Biomed. Eng.*, BME-31(10):644–651, 1984.
- [36] Michael Eberdt, Patrick K. Brown, and Gianluca Lazzi. Two-dimensional spice-linked multiresolution impedance method for low-frequency electromagnetic interactions. *IEEE Trans. Biomed. Eng.*, 50(7), 2003.

- [37] Stefan Schmidt, Carlos J. Cela, Vinit Singh, James Weiland, Mark S. Humayun, and G. Lazzi. *Artificial Sight*, chapter Computational Modeling of Electromagnetic and Thermal Effects for a Dual-Unit Retinal Prosthesis: Inductive Telemetry, Temperature Increase, and Current Densities in the Retina. Springer/AIP Press, 2007.
- [38] Yunan Han, Yinghua Lu, Jinling Zhang, and Biao Yang. A 3-d impedance method to compute current induced in human body exposure to power lines. In *Proc. Int. Symposium on Microwave, Antenna, Propagation and EMC Technologies for Wireless Communications*. IEEE, 2005.
- [39] John F. Deford and Om P. Gandhi. An impedance method to calculate currents induced in biological bodies exposed to quasi-static electromagnetic fields. *IEEE Transactions on Electromagnetic Compatibility*, EMC-27(3):168–172, 1985.
- [40] Vinit Singh, Ajeet Ajeet, Nitin Kwatra, Carlos J. Cela, John Ziriach, John D’Andrea, and Gianluca Lazzi. Computation of induced current densities in the human body at low frequencies due to contact electrodes using the adi-fdtd method. *IEEE Trans. Electromagn. Compat.*, (in press), 2010.
- [41] John Xie, Gene-Jack Wang, Lindy Yow, Carlos J. Cela, Mark S. Humayun, James Weiland, Gianluca Lazzi, and Hossein Jadvar. Modeling and percept of transcorneal electrical stimulation in humans. *IEEE Trans. Biomed. Eng.*, 2010 (in print).
- [42] R. C. Lee. Cell injury by electric forces. In R. C. Lee, F. Despa, and K. J. Hamann, editors, *Cell Injury: Mechanisms, Responses, and Repair*, volume 1066 of *Annals of the New York Academy of Sciences*, pages 85–91, 2005. Conference on Cell Injury - Responses and Repair, Chicago, IL, 2004.
- [43] N. Orcutt and O. P. Gandhi. A 3-d impedance method to calculate power deposition in biological bodies subjected to time-varying magnetic-fields. *IEEE Trans. Biomed. Eng.*, 35(8), 1988.
- [44] Mohammad Nadeem, Thorleif Thorlin, and Om P. Gandhi. Computation of electric and magnetic stimulation in human head using the 3-d impedance method. *IEEE Trans. Biomed. Eng.*, 50(7), 2003.
- [45] Victor Spitzer, Michael J. Ackerman, Ann L. Scherzinger, and David Whitlock. The visible human male: A technical report. *Journal of the American Medical Informatics Association*, 3(2), April 1996.
- [46] D. V. Thiel and R. Mittra. Self-consistent impedance method for the solution of electromagnetic problems. In *IEEE Microwave Conference, 2000 Asia-Pacific*, pages 281–285. IEEE, 2000.

- [47] J. Dongarra, A. Lumsdaine, R. Pozo, and K. Remington. A sparse matrix library in c++ for high performance architectures. In *Proceedings of the Second Object Oriented Numerics Conference*, pages 214–218, 1994.
- [48] Laurence Nagel and Ronald Rohrer. Computer analysis of nonlinear circuits, excluding radiation (cancer). *IEEE J. Solid-State Circuits*, 6(4):166–182, 1971.
- [49] Magdy F. Iskander, Mons D. Morrison, Wayne C. Datwyler, and Michael S. Hamilton. A new course on computational methods in electromagnetics. *IEEE Trans. Educ.*, 31(2), 1988.
- [50] S. Gabriel, R. W. Lau, and C. Gabriel. The dielectric properties of biological tissues: Iii. parametric models for the dielectric spectrum of tissues. *Phys. Med. Biol.*, 41:2271–2293, 1996.
- [51] C. J. Karwoski, D. A. Frambach, and L. M. Proenza. Laminar profile of resistivity in frog retina. *J. Neurophysiol.*, 54:1607–1619, 1985.
- [52] R. B. Beard, B. N. Hung, and Robert Schmuckler. Biocompatibility considerations at stimulating electrode interfaces. *Ann. Biomed. Eng.*, 20:395–410, 1992.
- [53] S. Gabriel, R. W. Lau, and C. Gabriel. The dielectric properties of biological tissues: Ii. measurements in the frequency range 10 hz to 20 ghz. *Phys. Med. Biol.*, 41:2251–2269, 1996.